Draft version October 16, 2015
Preprint typeset using LaTeX style emulateapj v. 5/2/11

arXiv:1401.5565v3 [astro-ph.HE] 14 Oct 2015

THE FIRST GAMMA-RAY BURSTS IN THE UNIVERSE

R. A. Mesler[1], Daniel J. Whalen[2,3], Joseph Smidt[2], Chris L. Fryer[4], N. M. Lloyd-Ronning[4] and Y. M. Pihlström[1]

Draft version October 16, 2015

ABSTRACT

Gamma-ray bursts (GRBs) are the ultimate cosmic lighthouses, capable of illuminating the universe at its earliest epochs. Could such events probe the properties of the first stars at $z \sim 20$, the end of the cosmic Dark Ages? Previous studies of Population III GRBs only considered explosions in the diffuse relic H II regions of their progenitors, or bursts that are far more more energetic than those observed to date. But the processes that produce GRBs at the highest redshifts likely reset their local environments, creating much more complicated structures than those in which relativistic jets have been modeled so far. These structures can greatly affect the luminosity of the afterglow, and hence the redshift at which it can be detected. We have now simulated Population III GRB afterglows in H II regions, winds, and dense shells ejected by the star during the processes that produce the burst. Our model, which has been used in previous work, has been extended to include contributions from reverse shocks, inverse Compton cooling and the effects of sphericity and beaming in the blast wave, and is valid in a variety of circumjet density profiles. We find that GRBs with $E_{\rm iso,\gamma} = 10^{51}$ - 10^{53} erg will be visible at $z \gtrsim 20$ to the next generation of near infrared and radio observatories. In many cases, the environment of the burst, and hence progenitor type, can be inferred from the afterglow light curve. Although some Population III GRBs are visible to *Swift* and the Very Large Array now, the optimal strategy for their detection will be future missions like EXIST and JANUS, which have large survey areas and onboard X-ray and infrared telescopes that can track their near infrared flux from the moment of the burst, thereby identifying its redshift.

Subject headings: gamma rays: bursts—early universe – galaxies: high-redshift – galaxies: star clusters – stars: early-type – stars:winds, outflows – supernovae: general – radiative transfer – hydrodynamics – black hole physics – cosmology:theory

1. INTRODUCTION

Gamma-ray bursts (GRBs) are the ultimate cosmic lighthouses, capable of illuminating the universe at its earliest times. They have now been detected at $z = 9.4$ (GRB 090423; Cucchiara et al. 2011), $z = 8.26$ (GRB 090423; Salvaterra et al. 2009), and $z = 6.7$ (GRB 080913; Greiner et al. 2009). Besides tracing star formation rates over cosmic time (e.g., Totani 1997; Wijers et al. 1998), GRBs can also constrain the metallicity and reionization history of the early IGM (e.g., Ioka 2003; Totani et al. 2006; Wang et al. 2012), the dark energy equation of state (e.g., Wang et al. 2011), and the properties of host galaxies (Barkana & Loeb 2004; Toma et al. 2011) (see also Bromm & Loeb 2006a, for a concise discussion of GRB cosmology).

Could GRBs also probe the properties of the first stars, and the environments in which they form? Population III (Pop III) stars are the key to understanding early cosmological reionization (e.g., Kitayama et al. 2004; Abel et al. 2007) and chemical enrichment (Smith & Sigurdsson 2007; Smith et al. 2009; Ritter et al. 2012; Safranek-Shrader et al. 2013), the properties of primeval galaxies (e.g., Jeon et al. 2012; Wise et al. 2012; Pawlik et al. 2013) and the origins of supermassive black holes (e.g., Whalen & Fryer 2012; Johnson et al. 2012, 2013b; Latif et al. 2013). Although numerical models (e.g., Bromm et al. 2009; Glover 2013; Whalen 2012; Hirano et al. 2013) and the fossil abundance record (Beers & Christlieb 2005; Frebel et al. 2005; Joggerst et al. 2010; Joggerst & Whalen 2011; Caffau et al. 2012; Keller et al. 2014) both suggest that Pop III stars are 30 - 500 $M_\odot$, there are, for now, no direct observational constraints on their masses.

Pop III GRBs might signal the deaths of the first stars because they are visible at very high redshifts. Gamma rays from long-duration GRBs can be detected by *Swift* out to $z \gtrsim 20$ (Lamb & Reichart 2000; Bromm & Loeb 2002, 2006b; Mészáros & Rees 2010). Analytical models suggest that GRB afterglows, which are required to pinpoint their redshifts, may be visible at $z \sim 15$ - 30 (Ciardi & Loeb 2000; Gou et al. 2004; Ioka & Mészáros 2005; Inoue et al. 2007; de Souza et al. 2011; Nakauchi et al. 2012; Kashiyama et al. 2013). These studies either did not have complete afterglow physics or only examined jets in uniform densities, like those of the H II regions of Pop III stars (Whalen et al. 2004)(but see Laskar et al. 2014, for a $z \sim 6$ GRB that is thought to have occurred in a uniform density).

But the processes that produce a GRB likely reset its local environment, creating far more complicated structures than those in which GRB jets have been modeled to date. These structures, such as multiple shocks and

[1] Department of Physics and Astronomy, University of New Mexico, Albuquerque, NM 87131
[2] T-2, Los Alamos National Laboratory, Los Alamos, NM 87545
[3] Universität Heidelberg, Zentrum für Astronomie, Institut für Theoretische Astrophysik, Albert-Ueberle-Str. 2, 69120 Heidelberg, Germany
[4] CCS-2, Los Alamos National Laboratory, Los Alamos, NM 87545

dense shells, can greatly affect the luminosity of the afterglow and hence the redshift at which it can be detected. The latest work has focused on the very energetic bursts (10^{55} - 10^{57} erg; Suwa & Ioka 2011; Nagakura et al. 2012) of 1000 $M_\odot$ Pop III stars. However, Pop III stars this massive have been rendered much less likely by the most recent primordial star formation models, and it is not clear if the proto-black holes of such stars have the energy densities required to launch GRB jets, given their large radii (Fryer et al. 2001; Fryer & Heger 2011).

To obtain more realistic light curves for Pop III GRBs in the near infrared (NIR), X-rays, and radio, and to determine more accurate limits in redshift for their detection, we have modeled the afterglows of these explosions for a variety of progenitors and ambient media. We also determine if the environment of the burst, and thus the properties of its progenitor, can be extracted from its light curves (e.g., Whalen et al. 2008a; Mesler et al. 2012). These calculations span the usual energies for both merger and single-star events, and our afterglow model produces light curves for relativistic jets in any density profile, not just the H II regions of earlier studies. Our simulation code is the one used in Mesler et al. (2012) (hereafter M12) but with significant improvements that include the contribution to the flux by inverse Compton scattering and reverse shocks, and the effects of beaming and the spherical nature of the blast wave.

We also revisit the question of whether or not collisions of GRB jets with large density jumps, like those associated with the massive structures ejected by some stars prior to the burst, can produce flares. Standard afterglow models predict flares for some collisions that are consistent with those observed in past events. Until recently, such features have usually been attributed to delayed energy injection from the central engine, not collisions. But some contend that collisions cannot produce flares because the extended emission region behind the blast wave and effects from reverse shocks tend to wash out bumps in the light curve (Gat et al. 2013). In this paper, we explore this problem in greater detail. As shown later, these effects (which our improved algorithm captures) mitigate flares but do not eliminate them, and some Pop III GRBs do exhibit prominent flares.

In Section 2 we review likely pathways for Pop III GRBs, and in Section 3 we examine the circumburst environments they create. We lay out our grid of simulations in Section 4 and in Section 5 we present x-ray, NIR, and radio light curves for Pop III GRBs in all of these environments and revisit the production of flares in some of these events. Detection strategies for Pop III GRBs are examined in Section 6. Our GRB light curve model is described in detail in the Appendix.

2. POP III GRB PROGENITORS

Long duration (LD) GRBs have been shown to be connected to the deaths of massive stars (e.g., Stanek et al. 2003) and to Type Ib/c supernovae in particular, whose progenitors have lost their hydrogen envelopes (Woosley & Bloom 2006). The leading contender for the central engines of LD GRBs is the collapsar model (Woosley 1993; MacFadyen et al. 2001), in which the core of a massive star collapses to a black hole (BH) accretion disk system that drives a relativistic jet through the outer layers of the star and into the surrounding medium. Besides the ejection of the hydrogen envelope, which is usually necessary for the jet to break out of the star, collapsars require stellar cores with unusually high angular momenta. In principle, any star that creates a black hole can make a GRB, but given the steep decline in the stellar IMF in galaxies today, most GRB progenitors are thought to be 40 - 60 $M_\odot$.

Two primary channels have been proposed for LD GRBs. In the first, a single rapidly rotating star sheds its outer envelope in some type of outburst, like a luminous blue variable (LBV) ejection (e.g., Baraffe et al. 2001), a Wolf-Rayet (WR) phase, or a pulsational pair instability (Heger & Woosley 2002; Whalen et al. 2014). In the second, the progenitor is in a binary when it becomes a red giant. The two stars enter a common envelope phase in which the second star is engulfed by the first and slowly spirals into its center, ejecting its outer envelope and spinning up its core in an exchange of angular momentum.

About a dozen pathways have been proposed in which a tightly-coupled binary system can collapse to form a BH accretion disk that powers a GRB, but they generally fall into two categories. In the first, the binary companion is another star (Fryer et al. 1999, 2007) and in the second it is a BH or neutron star (NS) (so-called He mergers; Fryer & Woosley 1998; Zhang & Fryer 2001). The key difference between the two is the time between the ejection of the envelope and the GRB. In the first, the H layer can be ejected as a dense shell up to several hundred kyr before the death of the star and have a radius of several pc at the time of the burst. In most cases, this shell will be beyond the reach of the jet. In the second, a slower, more massive shell is ejected only a few years before the orbit of the BH decays into the center of the star and forms an accretion disk. The shell may only be a few AU in radius at the time of the burst. In both cases, strong winds usually precede and follow the expulsion of the envelope.

The latest simulations suggest that Pop III GRBs may be produced by these pathways more frequently than previously thought. The discovery that fragmentation (e.g., Clark et al. 2011; Greif et al. 2012) and UV breakout (Hosokawa et al. 2011; Stacy et al. 2012) in primordial halos may limit the masses of some Pop III stars to $\lesssim$ 50 $M_\odot$ implies that more of them may fall into the mass range for GRBs than previously expected. It is also now known that Pop III stars can die as compact blue giants that are susceptible to outbursts or as red supergiants that can enter a common envelope phase, depending on the degree of convective mixing (Whalen et al. 2013f) or rotational mixing (Yoon & Langer 2005; Yoon et al. 2006) over the life of the star. The fact that some Pop III stars are now known to form in binaries (Turk et al. 2009) also improves the chances that some may enter a common envelope phase, a crucial ingredient for most collapsar scenarios. Finally, if many Pop III stars form with rotation rates that approach the breakup limit, as Stacy et al. (2011) suggest, more GRBs may have occurred relative to the number of massive stars at very high redshifts than today (although studies have shown that even at the critical velocity the cores of massive stars must often be spun up to even higher rates by a common envelope phase to produce collapsars; Fryer & Heger 2005).

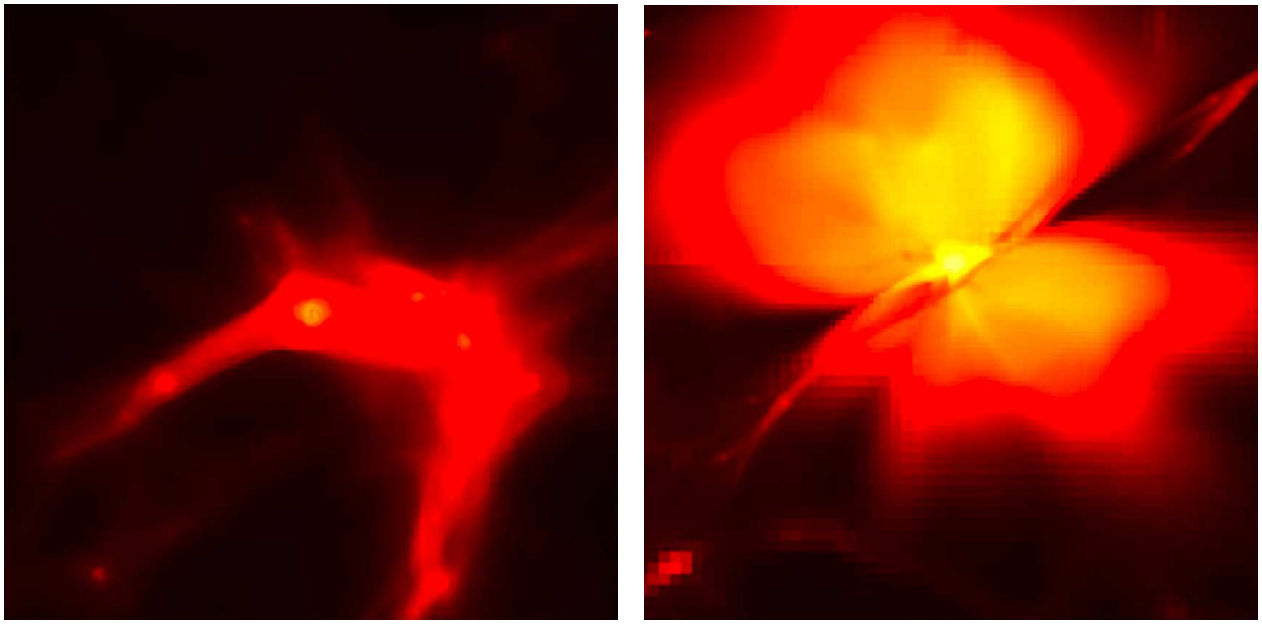

FIG. 1.— The environments of Pop III star formation and GRBs. Left: temperature image of an 8.0×10^5 $M_\odot$ primordial halo at $z = 16.8$. Right: temperature image of the H II region of a 100 $M_\odot$ Pop III star in the halo 2 Myr later. The image size is 4 kpc on a side.

3. THE ENVIRONMENTS OF POP III GRBS

Because Pop III stars are very massive, they usually ionize the halos that gave birth to them, creating H II regions 2.5 - 5 kpc in radius and driving all the gas from the halo in shocked flows on timescales of ~ 2 Myr (e.g., Whalen et al. 2004). In Figure 1 we show the H II region of a 100 $M_\odot$ star in a 8.0×10^5 $M_\odot$ halo at $z = 16.8$ that was simulated with the *Enzo* code. These flows create uniform density profiles with $n \sim 0.1$ - 1 cm^{-1} that extend 50 - 100 pc from the star, as shown in Figure 2. For this reason, and because Pop III stars are not thought to drive strong winds because they lack metals, previous studies have taken the GRB jet to propagate into uniform H II region densities. In the past, with less detailed observations, such profiles have yielded afterglow light curves that are in reasonable agreement with those of GRBs in the local universe.

In reality, the ejection of the envelope and the fast winds that accompany most GRBs reset the environment in the vicinity of the star. This holds true even for Pop III stars because the ejection of the envelope is driven by kinematics, not metallicity, and the He core would still drive a wind after the ejection because rotational and convective mixing enrich the core with metals. If the progenitor is a single star with an LBV outburst, the envelope would be a fast wind driving a slow shell into a uniform H II region. Collimated flows can complicate this picture. If less mass is blown along the axis of the star (and hence the jet) than its equator, the density along the axis will be intermediate to those of the H II region and the shell. Typical LBV outbursts expel 1 - 10 $M_\odot$ shells.

If the GRB is instead created by a merger in which the companion is a star, the envelope would just be a power-law wind profile, since in most cases the shell will be driven beyond the reach of the jet by the time of the burst. If the companion is a BH or NS, the shell will be much closer to the star at the time of the burst. Indeed, population synthesis models predict the average radius of shells expelled by He mergers to be 1 - 2 AU (see Figure 11 of Fryer et al. 2013, for $Z = 0.1$ $Z_\odot$ stars). However, the bulk of the envelope tends to be ejected along the equatorial plane of the progenitor in such events, so the density profile can again be intermediate to that of the H II region and a fast wind pushing a massive shell (see Figure 6 of Passy et al. 2012). We note that the jet can encounter clumps even if little of the envelope is expelled along the axis of the burst because violent insta-

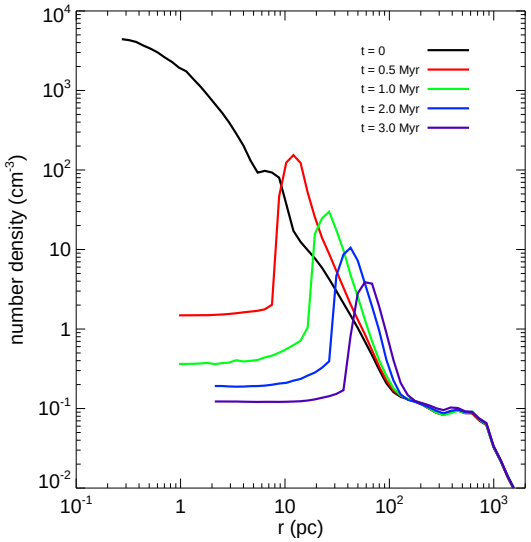

FIG. 2.— Spherically-averaged baryon density profiles for the H II region of a 100 $M_\odot$ Pop III star. Shocked, ionized core flows pile most of the baryons in the halo into a dense shell of radius ~ 100 pc by the end of the life of the star. Note that a second, smaller halo that is about to merge with the halo hosting the star is visible as the density bump at ~ 10 pc at $t = 0$, the time that the star is switched on.

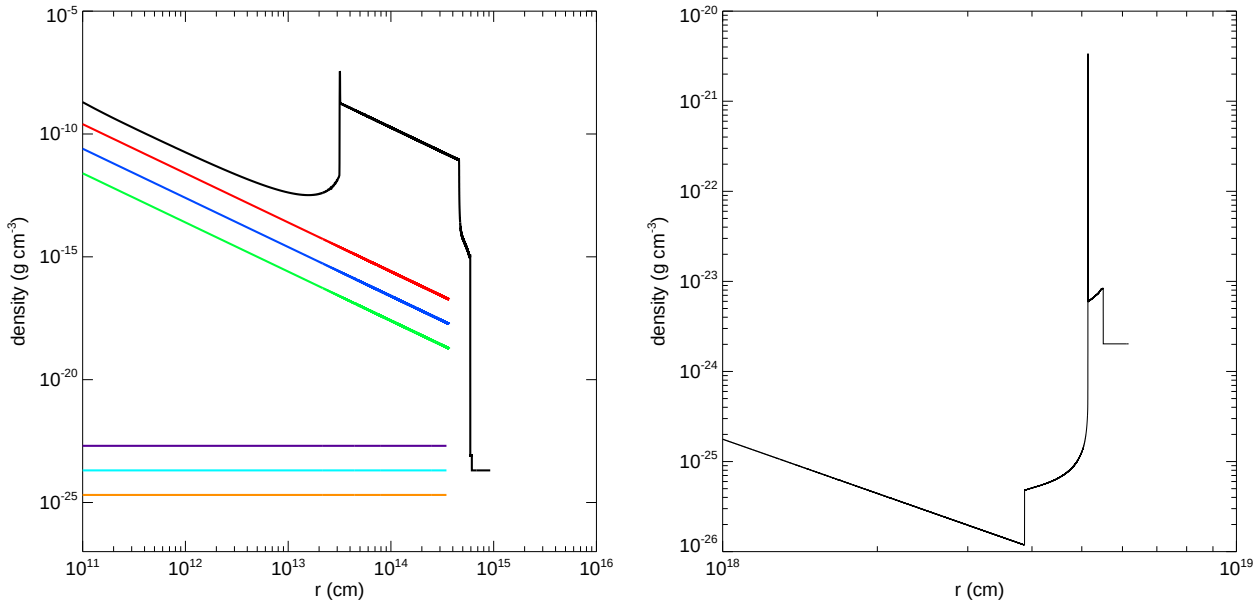

FIG. 3.— Circumburst profiles in our Pop III GRB survey. Left: density profiles for a 5 $M_\odot$ shell ejected by a He merger at 1.5 AU (black). Also included are 3 simple power-law winds (red: 10^{-4} $M_\odot$ yr^{-1}; blue: 10^{-5} $M_\odot$ yr^{-1}; green: 10^{-6} $M_\odot$ yr^{-1}) and three uniform H II regions (violet: 10 cm^{-3}; cyan: 1.0 cm^{-1}; brown: 0.1 cm^{-3}). Right: density profile of a 1 $M_\odot$ shell at $\sim$ 1 pc that was ejected in a binary merger 2000 yr prior to the burst.

bilities can form in the H II region of the star that leave dense fragments in its vicinity at the time of its death (Whalen & Norman 2008a,b).

In sum, the environments of Pop III GRBs fall into four basic categories:

1. the power-law density profile of a fast wind in which a shell has been driven beyond the reach of the GRB jet:

$$\rho_{\rm w}(r) = \frac{\dot{m}}{4\pi r^2 v_{\rm w}}, \quad (1)$$

where $\dot{m}$ is the mass loss rate of the wind and $v_{\rm w}$ is its speed. This profile is formed in most binary mergers between two stars and some single collapsars.

2. a fast wind driving a massive shell into a Pop III H II region, where the shell is at $\sim$ 0.2 pc at the time of the burst. This profile is created by some single collapsars and the relatively few mergers between two stars that place a shell within the range of the jet at the time of the burst.

3. a fast wind pushing into a massive shell in an H II region in which the inner surface of the shell is at 1 - 2 AU at the time of the burst. This is the profile of a He merger.

4. a diffuse, uniform H II region profile that a jet might encounter along certain lines of sight, such as in a toroidal mass ejection. This envelope is also appropriate for the much more massive and energetic GRBs considered by Suwa & Ioka (2011) and Nagakura et al. (2012), in which the star collapses without ejecting a shell.

4. POP III GRB MODELS

We consider GRBs in 12 density profiles. Three are simple winds, with $\dot{m} = 10^{-4}$, 10^{-5} and 10^{-6} $M_\odot$ yr^{-1}. Three are profiles in which a 5 $M_\odot$ shell is driven by a 10^{-5} $M_\odot$ yr^{-1} wind out to $\sim$ 0.2 pc in H II region densities of 0.1, 1.0 and 10 cm^{-3}. Three are profiles for He mergers, in which a 5 $M_\odot$ shell is driven by a 10^{-5} $M_\odot$ yr^{-1} wind into the same 3 H II regions above but only to a distance of $\sim$ 1.5 AU. The last three profiles are just the 3 H II regions themselves. In all cases, we take $v_{\rm w}$ = 2000 km s^{-1}, $v_{\rm shell}$ = 200 km s^{-1}, and the composition of the envelopes to be primordial, 76% H and 24% He by mass. We show density profiles for all our models in Figure 3.

Much higher energies ($E_{\rm iso,\gamma}$ = 10^{55} - 10^{57} erg) are sometimes invoked for Pop III GRBs in part because the mass of the star, and hence the reservoir of gas that is available to the central engine, is thought to be much greater than in stars today. Suwa & Ioka (2011) and Nagakura et al. (2012) also find that such energies are required for the jet to punch through the outer layers of very massive stars that do not shed their hydrogen envelopes. We proceed under the assumption that most Pop III GRBs are similar to those today and consider the usual energies for such events, 10^{51}, 10^{52}, and 10^{53} erg. There are thus a total of 36 models in our simulation campaign. For simplicity, we take the initial Lorentz factor of the jet, Γ_0, to be 500, and the duration of the burst in the Earth frame to be 100 seconds. We take all the explosions in our study to occur at $z = 20$.

4.1. *ZEUS-MP Outburst Models*

We calculate density profiles for outbursts in Pop III H II regions with ZEUS-MP (Whalen & Norman 2006) in the same manner as in M12. We treat stellar winds and

Instrument	Frequency Range		Sensitivity	Integration Time
	Min (GHz)	Max (GHz)	(mJy)	(minutes)
LWA	1.0×10^{-2}	8.8×10^{-2}	1.0×10^{-1}	4.8×10^{2}
LOFAR	3.0×10^{-2}	8.0×10^{-2}	8.0×10^{-1}	4.8×10^{2}
VLA	1.0	4.0×10^{1}	2.5×10^{-2}	3.6×10^{2}
SKA	0.1	1.0×10^{2}	5.0×10^{-4}	1.7×10^{1}
ALMA	8.4×10^{1}	7.2×10^{2}	3.5×10^{-2}	3.6×10^{2}
GRIPS IRT	1.0×10^{4}	4.0×10^{4}	9.3×10^{-4}	8.3×10^{0}
JWST NIRcam	6.3×10^{4}	4.3×10^{5}	1.0×10^{-4}	1.7×10^{2}
WFIRST	1.5×10^{5}	4.0×10^{5}	2.6×10^{-4}	1.7×10^{1}
JANUS NIRT	1.8×10^{5}	4.3×10^{5}	6.7×10^{-2}	8.0×10^{0}
EXIST IRT	1.3×10^{5}	1.0×10^{6}	2.3×10^{-3}	5.0×10^{-1}
SVOM MXT	7.3×10^{7}	1.5×10^{9}	4.3×10^{-3}	1.7×10^{-1}
SVOM ECLAIRS	9.7×10^{8}	6.0×10^{10}	3.9×10^{-2}	1.7×10^{1}
LOBSTER WF XRT	1.2×10^{8}	3.6×10^{9}	5.6×10^{-3}	5.0×10^{-1}
JANUS XRFM	1.2×10^{8}	6.0×10^{9}	7.0×10^{-2}	5.0×10^{-1}
EXIST HET	1.2×10^{9}	3.6×10^{10}	1.9×10^{-3}	1.7×10^{0}
Swift BAT	3.6×10^{9}	3.6×10^{10}	1.9×10^{-4}	1.7×10^{0}
Fermi GBM	2.4×10^{9}	6.0×10^{12}	3.1×10^{-5}	1.7×10^{0}

TABLE 1
Frequency ranges and sensitivities for some current and proposed radio, infrared, and X-ray instruments. All sensitivities are at the 5σ level for the given integration time.

outbursts as time-dependent inflows at the inner boundary of a one-dimensional (1D) spherical grid:

$$\rho = \frac{\dot{m}}{4\pi {r_{\rm ib}}^2 v_{\rm w}}, \quad (2)$$

where $r_{\rm ib}$ is the radius at the inner boundary and $v_{\rm w}$ is the wind velocity. Outbursts are generated by increasing $\dot{m}$ and lowering $v_{\rm w}$. At the beginning of a run the grid is initialized with one of the 3 H II region densities. The mesh has 32,000 uniform zones and extends from 3.084 $\times$ 10^{10} cm to 9.252 $\times$ 10^{14} cm ($\sim$ 60 AU) for He merger simulations and from 10^{-5} pc to 0.2 pc for other mergers. We impose outflow conditions on the outer boundary, and the grid is domain decomposed into 8 tiles, with 4000 zones per tile and one tile per processor.

Radiative cooling can flatten shells into cold, dense structures that strongly affect the evolution of the GRB jet. Although there are no metals or dust in our primordial ejections the shell can still cool by x-ray emission and H and He lines in the shocked gas. Our ZEUS-MP models include collisional excitation and ionization cooling by H and He, recombinational cooling, H_2 cooling, and bremsstrahlung cooling, with our nonequilibrium H and He reaction network providing the species mass fractions (H, H^+, He, He^+, He^{2+}, H^-, H_2^+, H_2, and e^-) needed to calculate these collisional cooling processes. The hydrodynamics in our models is always evolved on the lesser of the cooling and Courant times to capture the effect of cooling on the structure of the flow. We neglect the effect of ionizing radiation from the progenitor on winds and shells. This treatment is approximate, given that the star illuminates the flow and that its luminosity evolves over time. However, the energy deposited in the flow by ionizations is small in comparison to its bulk kinetic energy and is unlikely to alter its properties in the vicinity of the burst.

One important difference between our shell profiles and those of M12 is that a fast wind does not precede the ejection of the envelope and later detach from its outer surface to create a very low-density rarefaction zone ahead of the shell. The outburst instead plows up the much higher density H II region, as shown in Figure 3. Note that there are significant differences in the structures of shells ejected just before the burst and ejections 2000 yr before the burst. Radiative cooling has inverted the density profile inside the shell at later times and created a much larger density jump at the interface between the shell and the termination shock due to the wind that piles up at its inner surface. These structural differences, together with the distance of the shell from the explosion, have important consequences for GRB light curves as we discuss below.

5. POP III GRB LIGHT CURVES

We tabulate frequency bands and sensitivities for current and proposed radio, NIR, and X-ray instruments in Table 1. The radio instruments include the Long Wavelength Array (LWA; Taylor et al. 2012), the Low Frequency Array (LOFAR)[5], the Very Large Array (VLA)[6], the Square Kilometer Array (SKA)[7], and the Atacama Large Millimeter Array (ALMA)[8]. The NIR instruments are the GRB Investigation via Polarimetry and Spectroscopy Infrared Telescope (GRIPS IRT; Greiner et al. 2012), the *James Webb Space Telescope* (*JWST*) NIR Camera (NIRCam)[9], the Wide-Field Infrared Survey Telescope (WFIRST; Spergel et al. 2013), the Joint Astrophysics Nascent Universe Satellite NIR Telescope (JANUS NIRT; Burrows et al. 2010), and the Energetic X-ray Imaging Survey Telescope Infrared Telescope (EXIST IRT; Grindlay 2010). The X-ray instruments include the Space-based Variable Objects Monitor (SVOM) Micro-channel X-ray Telescope (MXT) and ECLAIRs (Paul et al. 2011), the Large Angle Observa-

[5] http://www.astron.nl/radio-observatory/astronomers/lofar-imaging-capabilities-sensitivity/sensitivity-lofar-array/sensiti
[6] https://science.nrao.edu/facilities/vla/docs/manuals/propvla/determining/source
[7] http://www.astron.nl/radio-observatory/astronomers/lofar-imaging-capabilities-sensitivity/sensitivity-lofar-array/sensiti
[8] http://almascience.eso.org/proposing/sensitivity-calculator
[9] http://www.stsci.edu/jwst/instruments/nircam/sensitivity

tory with Energy Resolution (LOBSTER) Wide-Field X-ray Telescope (WF XRT; Gorenstein 2011), the JANUS X-ray Flash Monitor (XRFM; Falcone et al. 2009), the EXIST High-Energy Telescope (HET; Hong et al. 2009), and the *Swift* Burst Alert Telescope (BAT) and *Fermi* Gamma-ray Burst Monitor (GBM)[10].

5.1. *H II Regions*

We show afterglow light curves for Pop III GRBs in uniform-density H II regions at $z = 20$ in Figure 4. In all three plots sensitivity limits are shown for the appropriate instruments, beginning at the minimum integration time for each one that would result in a detection. The peak flux occurs at later times for lower frequencies. Fluxes are highest in the NIR, reaching ~ 10 mJy for a 10^{53} erg burst in an $n = 10$ cm^{-3} H II region. They are somewhat lower in the radio and X-ray, although the radio flux falls off only gradually after reaching its peak. In the NIR and X-ray, the flux scales roughly with the burst energy, but in the radio the flux increases by a factor of ~ 50 with each decade in energy. Also, the NIR and X-ray afterglows are brightest in the highest densities at early times, but after a few hours this trend is reversed. There is much less variation in flux with ambient density in the radio afterglows.

The peak flux at a given frequency is greatest in the NIR at ~ 3 μm, and it decreases monotonically above and below this frequency. Pop III GRB afterglows in H II regions will thus most easily be detected in current and proposed NIR instruments. The afterglow reaches a peak at or before $\sim 10^{-1}$ days but falls off gradually enough that instruments such as GRIPS and WFIRST could detect a 10^{51} erg burst for up to about two days and a 10^{53} erg burst for up to 10 days. The JANUS NIRT would detect a 10^{53} erg burst for about ten days, while a 10^{51} erg burst would be just at the threshold of detectability. The EXIST IRT would see NIR afterglows for 0.5 - 25 days at $z \sim 20$, and *JWST* could detect these events for 2 - 80 days, depending on energy and H II region density.

In the radio portion of the spectrum, the VLA could just barely detect a 10^{51} erg burst in a 0.1 cm^{-3} H II region, while the the same burst would be visible to the SKA for about an hour. At the opposite extreme, a 10^{53} erg GRB in a 10 cm^{-3} H II region would be detectable by the VLA for nearly 80 days while SKA would see the same afterglow for ~ 200 days. Because the peak flux is reached earlier at higher frequencies, it will be difficult for ALMA to detect even the brightest afterglow for more than about a day. LOFAR will not see these explosions because its sensitivity falls below their peak fluxes. At 80 MHz, the peak flux only reaches $\sim 10^{-2}$ mJy, well below the LOFAR 5σ sensitivity of 80 mJy for an eight hour integration.

GRBs in H II regions do not produce very bright X-ray afterglows. The X-ray instruments that are sensitive to the lowest frequency X-rays will be the most suitable for detecting these events. The MXT, HET, and WFI aboard SVOM, EXIST, and LOBSTER, respectively, plus the GBM on Fermi, with their high sensitivities and low minimum observable frequencies, will most

[10] http://fermi.gsfc.nasa.gov/science/mtgs/symposia/2012/program/tue/PJenke.pdf

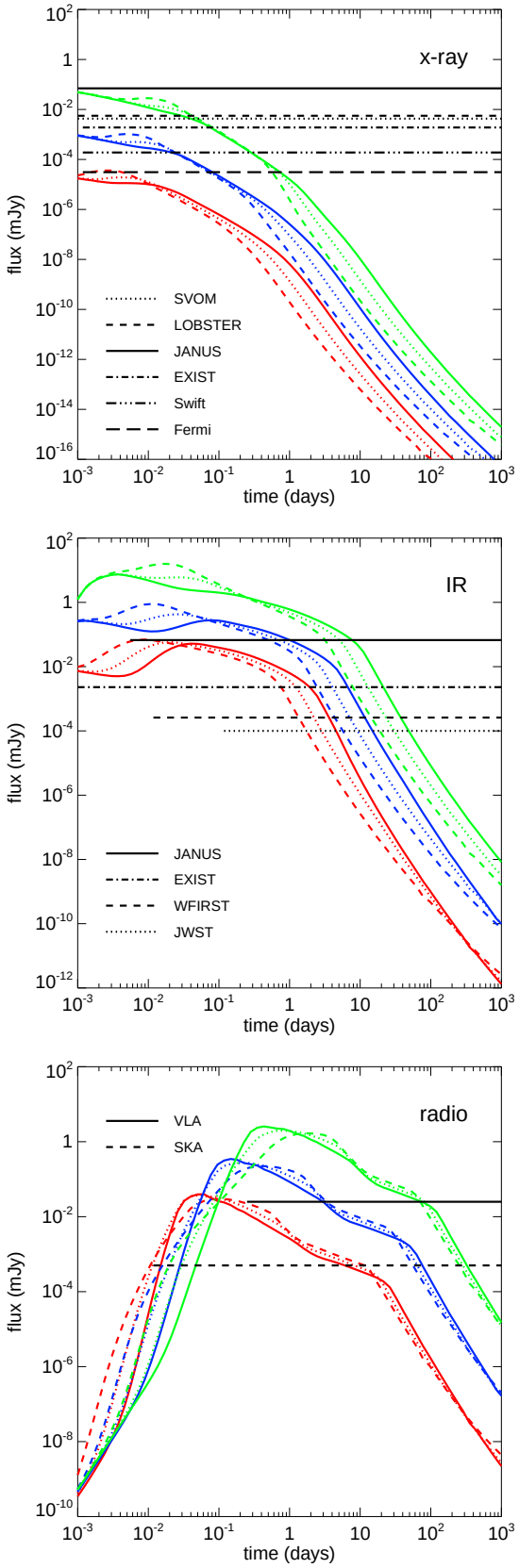

FIG. 4.— Afterglow light curves for Pop III GRBs in uniform H II regions for $E_{\rm iso,\gamma} = 10^{51}$ erg (red), 10^{52} erg (blue), and 10^{53} erg (green). Top: X-ray (82.7 keV); center: NIR (3.0 μm); bottom: radio (5 GHz). Solid: $n = 0.1$ cm^{-1}; dotted: $n = 1.0$ cm^{-1}; dashed: $n = 10$ cm^{-1}. All times are in the earth frame.

easily detect Pop III GRBs. Only the bursts with the highest energies would be visible. A 10^{51} erg GRB would reach a maximum flux of only $\sim 10^{-4}$ mJy at 3×10^9 GHz, well below the detection thresholds of every current and proposed X-ray mission except for the Fermi GBM. But a 10^{53} erg event could produce an afterglow with a flux of $\sim 10^{-1}$ mJy at 10^9 GHz immediately after the end of the prompt emission phase. This flux would then fall off slowly enough for SVOM, EXIST, and LOBSTER to detect the afterglow for nearly a day. We note that the FERMI LAT is not well suited to hunting for high-redshift GRB afterglows because of its high threshold frequency, 4.8×10^{12} GHz, and modest sensitivity.

5.2. *Winds*

Light curves for GRBs in r^{-2} winds are shown in Figure 5. As noted earlier, these environments are expected in many binary merger scenarios in which the hydrogen envelope of the star has been driven by stellar winds to radii that are beyond the reach of the jet before its afterglow dims below visibility. Like GRBs in H II regions, afterglows from explosions in stellar winds are brightest in the NIR at about 3.0 μm, with peak fluxes falling off above and below this frequency. However, due to the higher densities at smaller radii, afterglow fluxes at frequencies above the radio are greater in winds than in H II regions for a given burst energy. But fluxes in the radio are dimmer in winds than in H II regions because they peak at later times, when the jet is at larger radii and lower densities than the H II regions. All three fluxes scale roughly with the energy of the burst after a few hours, when the brightest afterglows are generally in the most diffuse envelopes.

A 10^{53} erg burst in a 10^{-4} $M_\odot$ yr^{-1} wind reaches a maximum NIR flux of ~ 1 Jy 100 seconds after the burst, making it readily detectable for up to 10 days with EXIST. GRIPS and WFIRST could extend this window out to 10 - 20 days, and this event would be visible to JANUS NIRT for almost a day. JANUS, however, with its somewhat lower sensitivities, would not be able to see the lowest energy bursts in the NIR because their fluxes fall so quickly after the burst. But EXIST would see these GRBs for up to half a day. The most sensitive of the instruments, the *JWST NIRCam*, could observe the least energetic GRBs for a day and the most energetic ones for 100 days, providing detailed followup to an initial detection in X-rays.

Besides being somewhat dimmer than in H II regions, radio afterglows in winds reach peak fluxes at later times, 1 - 30 days instead of 0.1 - 3 days. The radio flux also peaks at later times in higher mass loss rates. A 10^{53} erg burst in a 10^{-6} $M_\odot$ yr^{-1} stellar wind reaches a peak flux of ~ 1 mJy at 5 GHz after 0.8 days. It would be possible to detect such an afterglow with the VLA from about 0.1 - 80 days after the burst, and SKA would extend this range out to 200 days. Neither ALMA nor LOFAR would be able to detect a Pop III GRB afterglow at $z = 20$ in a stellar wind. The least energetic GRBs in the strongest winds are marginally detectable by VLA for a day and would be visible to SKA for about 10 days.

X-ray afterglows for GRBs in stellar winds are much brighter than those H II regions. A 10^{53} erg GRB at $z = 20$ produces fluxes greater than 20 mJy at 10^9 GHz for 2.5 hours. This emission would be easily de-

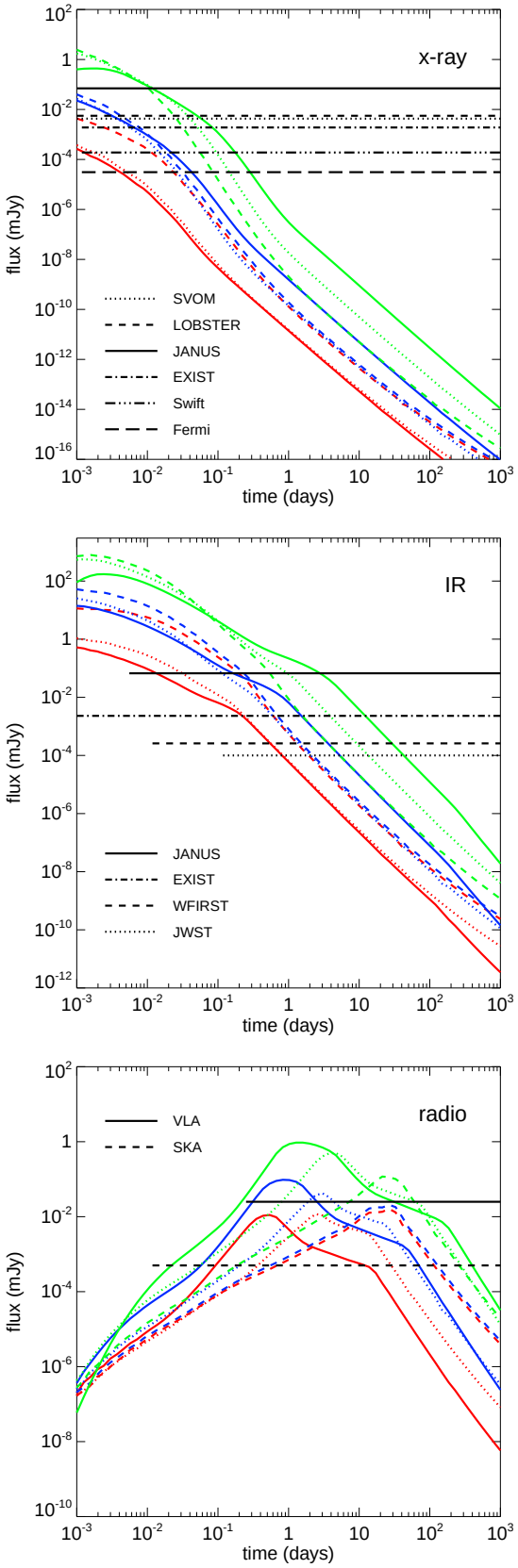

FIG. 5.— Afterglow light curves for Pop III GRBs in r^{-2} wind profiles for $E_{\rm iso,\gamma} = 10^{51}$ erg (red), 10^{52} erg (blue), and 10^{53} erg (green). Top: X-ray (82.7 keV); center: NIR (3.0 μm); bottom: radio (5 GHz). Solid: $\dot{m} = 10^{-6}$ $M_\odot$/yr; dotted: $\dot{m} = 10^{-5}$ $M_\odot$/yr; dashed: $\dot{m} = 10^{-4}$ $M_\odot$/yr. All times are in the earth frame.

tectable by SVOM, EXIST, LOBSTER, JANUS, Swift, and the *Fermi* GBM. The afterglow would be visible to the JANUS XRFM for nearly a half an hour and to *Fermi* for almost two hours. At the other extreme, a 10^{51} erg GRB in a 10^{-6} $M_\odot$ yr^{-1} wind would produce an afterglow that would only reach $\sim 5 \times 10^{-3}$ mJy at 10^9 GHz. This event would only be detectable for $\sim$ 200 seconds with the *Fermi GBM*, and would likely not be found by other instruments.

5.3. *He Mergers*

We show X-ray, NIR and radio light curves for Pop III GRB jets crashing into massive shells ejected by helium merger events in Figure 6. In each case the 5 $M_\odot$ shell, which has been driven into H II region densities of 0.1, 1, or 10 cm^{-3} by a stellar wind with $\dot{m} = 10^{-3}$ $M_\odot$ yr^{-1}, has a radius of $\sim$ 2 AU. The GRB jet breaks out into the r^{-2} wind before colliding with the shell. The high densities in the wind at these small radii decelerate the jet to mildly-relativistic speeds in $\sim$ 10 minutes in the local frame. Because the time between the ejection of the shell and the burst is short, the wind has not had time to pile up and form a termination shock at the inner layer of the shell. The jet therefore transitions directly from the wind to the hydrogen shell.

A mildly relativistic reverse shock forms at the contact discontinuity between the wind and the shell, which then steps back through the jet in the frame of the jet. A new forward shock develops with a lower Lorentz factor than that of the original forward shock but that is still, in general, mildly relativistic. The new forward shock advances into the shell and immediately encounters another density jump, where it produces another pair of forward and reverse shocks. This cycle continues, with several to dozens of shock pairs eventually being formed. By the time the first forward shock reaches the interior of the shell, where the density is nearly constant and no more shocks are produced, all forward shocks have become non-relativistic and all reverse shocks have retreated through the forward shocks that created them.

The jet remains in the shell for the entire 100 day simulation. When it finally emerges, there may be a slight re-collimation of the jet due to the low density of the surrounding medium. Any rebrightening of the light curve would be minimal however, due to the low density of the medium. We find that the H II region density beyond the shell has essentially no effect on the afterglow light curve because the structure of the shell has not yet been altered by the relic H II region.

Light curves for Pop III GRBs in He merger shells are quite different from those in winds and H II regions. Their structure in a given band varies strongly with the energy of the burst and also across the bands themselves. They also exhibit much more variation over time, with sharp drops that are sometimes preceded by flares. The peak flux is again in the NIR, but there is also a large initial X-ray flux. Radio emission is suppressed by synchrotron self-absorption in the high densities in the shell, so detecting He merger GRBs at any frequency below the IR will be nearly impossible with current or proposed instruments. The flux at all frequencies is essentially quenched a short time after the jet enters the shell.

The high densities in the shell (black plot in the left panel of Figure 3) produce a large NIR flux. A 10^{51} erg

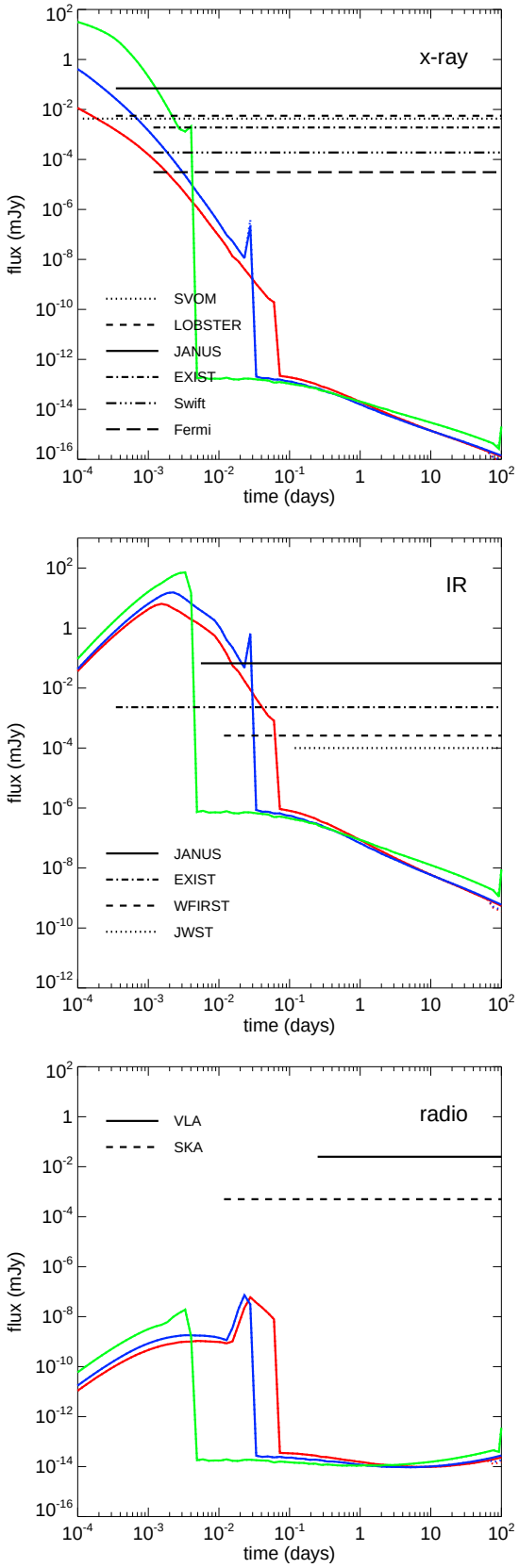

FIG. 6.— Afterglow light curves for Pop III GRBs in 5 $M_\odot$ shells at 2 AU that were ejected in He mergers. $E_{\rm iso,\gamma} = 10^{51}$ erg (red), 10^{52} erg (blue), and 10^{53} erg (green). Top: X-ray (82.7 keV); center: NIR (3.0 μm); bottom: radio (5 GHz). Solid, dotted and dashed lines are for shells expanding in ambient densities $n = 0.1$, 1.0, and 10 cm^{-1}, respectively. All times are in the earth frame.

GRB reaches a peak flux of 10 mJy at 150 seconds at 3.0 μm, while a 10^{53} erg GRB peaks at nearly 100 mJy. Although they are visible to all the NIR detectors in Table 1, they will probably only be detected by satellites whose onboard X-ray instruments are triggered by the event because their NIR fluxes are so short-lived. There would not be enough time to slew any ground-based instruments to capture the NIR afterglows of GRBs due to He mergers. This problem would be mitigated in cases in which there is more time between the ejection and the burst, since delays of up to several days would not alter the structure of the shell but would allow followup in the NIR from the ground. Note that fluxes from more energetic bursts are quenched sooner because the jet reaches the shell in less time. Higher burst energies imply larger ejecta masses for a given Lorentz factor, and they are not decelerated by the wind as much as jets with lower masses.

At 83 keV, the flux from a 10^{53} erg burst reaches 10 mJy just after the end of the prompt emission phase. This GRB would be visible to SVOM, JANUS, LOBSTER, EXIST, and *Fermi* until the jet collides with the shell at $t_{\rm obs} \lesssim 0.1$ days. The flux then drops by many orders of magnitude, in some cases after producing a flare that lasts for a few seconds to a few minutes. GRB afterglows with strong, transient X-ray and IR fluxes that end within a few hours would be clear signatures of a Pop III GRB from a He merger, particularly if there are flares.

5.4. *Binary Mergers*

We plot afterglow light curves for Pop III GRBs in dense shells ejected in binary mergers in Figure 7. The hydrogen shell has a mass of 5 $M_\odot$ and is driven to a radius of ~ 0.2 pc by a 10^{-5} $M_\odot$ yr^{-1} wind in H II region densities of 0.1, 1, and 10 cm^{-3}. The jet initially breaks out into the wind and then reaches the termination shock at about 10 days, where the wind has piled up at the inner surface of the shell. By this time the jet has decelerated to $\Gamma \sim 10$. A mildly relativistic reverse shock forms at the interface of the free-streaming and shocked winds and then propagates back into the jet. At the same time, a mildly relativistic forward shock advances into the shocked wind. As with the He merger shell, a series of forward and reverse shock pairs form at the interface between the free-streaming and shocked winds until the leading forward shock has fully advanced into the piled-up wind at the inner surface of the shell. The jet, now only mildly relativistic, reaches the shell itself at several hundred to 1000 days, at which time it becomes non-relativistic. A series of shock pairs are again created as the jet enters the shell as in the He merger case. The jet eventually breaks out of the hydrogen shell and into the H II region, but only after several thousand days.

As shown in Figure 7, the afterglow light curves are similar to those in stellar winds out to 20 - 50 days. Although the jet collides with the shocked wind after ~ 5 days, the effect on the light curve is minimal. Only when the jet reaches the hydrogen shell at 20-50 days does the light curve deviate from that of a simple wind. In the X-ray band, the afterglow falls below the detection limits of current and proposed instruments before the jet collides with the shell. In the IR, the flux is only $10^{-5}-10^{-4}$ mJy when the shell is reached, making the transition into the

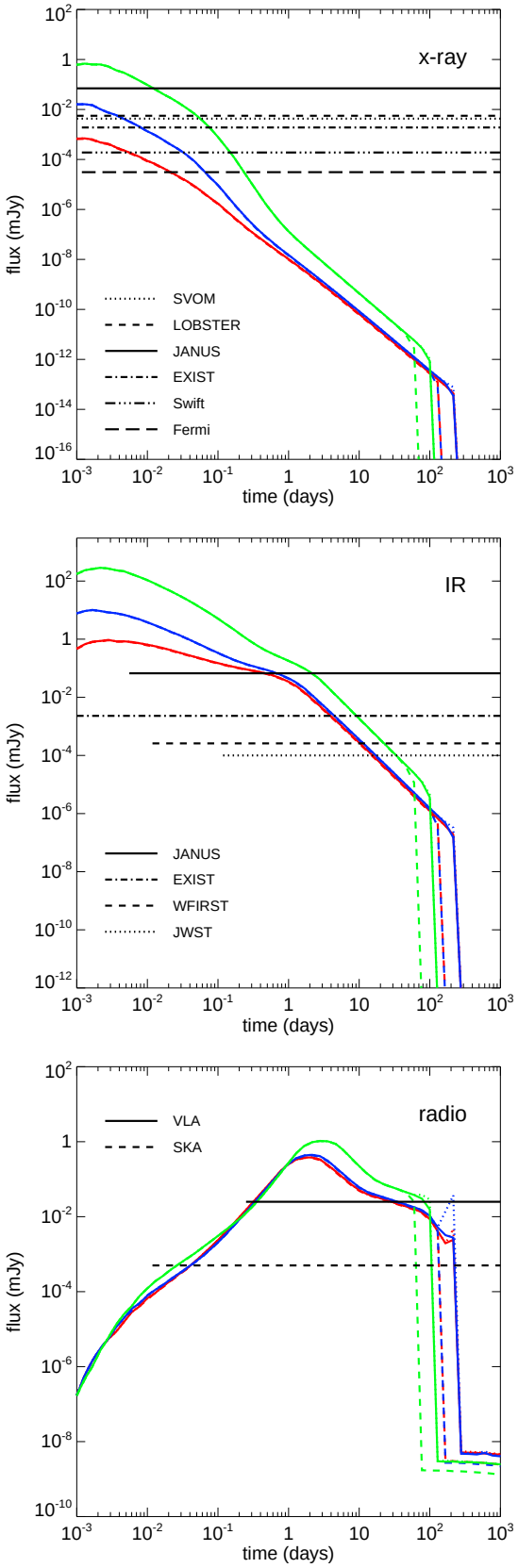

FIG. 7.— Afterglow light curves for Pop III GRBs in 5 $M_\odot$ shells at 0.2 pc ejected in binary mergers. $E_{\rm iso,\gamma} = 10^{51}$ erg (red), 10^{52} erg (blue), and 10^{53} erg (green). Top: X-ray (82.7 keV); center: NIR (3.0 μm); bottom: radio (5 GHz). Solid, dotted and dashed lines are for shells expanding in ambient densities $n = 0.1$, 1.0, and 10 cm^{-1}, respectively. All times are in the earth frame.

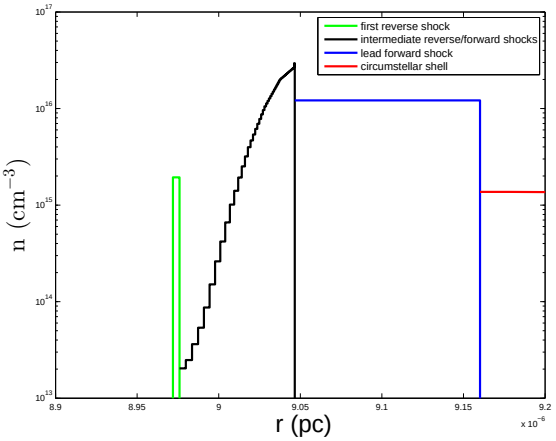

FIG. 8.— Density structure of the jet after it has collided with the dense shell. The red region is the local density of the shell at the leading edge of the jet. The blue region marks the leading forward shock created by the interaction of the jet with the most recent density jump. This shock advances into the shell ahead of the rest of the jet. The black region shows the series of forward and reverse shock pairs that were formed as the jet collides with the shell. The spike (green) at the rear of the jet is the ambient material swept up before the jet reaches the shell. The reverse shock that formed when the jet with the shell has backstepped past the initial forward shock.

shell barely detectable with *JWST* or perhaps WFIRST, and then only for the most energetic bursts. Likewise, at 5 GHz the afterglow flux is only $\sim 10^{-2}$ mJy when the jet crashes into the shell. The VLA may barely be able to detect the sudden drop in flux when the jet collides with the shell, but the SKA will detect it. Note that in some cases the drop in flux will be preceded by a flare in the radio. Pop III GRBs due to binary mergers would look like events in simple winds, even when the shell is relatively close to the progenitor because the X-ray and NIR fluxes would fall below detectability before plummeting when the jet reaches the shell. However, they could still be distinguished from GRBs in winds by followup observations in the radio at later times, which could capture the abrupt drop in flux. Even the least energetic Pop III GRB from a binary merger will be visible in the NIR to all the instruments in Table 1 for at least a day.

Our models show that what primarily governs the light curves of Pop III GRBs due to He and binary mergers for a given energy are the mass loss rates after the ejection (and hence the density of the wind envelope) and the time between the ejection and the burst. The mass of the shell does not matter, as long as it can fully quench the jet.

5.5. *Flares*

At least half of GRBs with observed afterglows exhibit some sort of flaring in their light curves (see, e.g., Roming et al. 2012). The leading contender for the origin of these flares is late-time central engine activity. The collision of the relativistic jet with strong density features has also been suggested as the cause of some flares, like those in our He and binary merger models (M12). But some have questioned if flares really occur when a GRB jet collides with a dense shell (Gat et al. 2013). When the jet encounters the shell, a pair of forward and reverse shocks is formed, as noted earlier. The new forward shock continues into the shell while the reverse shock steps back through the old forward shock in the frame of the shock. Material swept up by the new forward shock does not mix with material that was swept up prior to the collision because of the contact discontinuity between the reverse shock and the new forward shock. The M12 afterglow model, which employs the swept mass approximation to model jet evolution, may therefore overestimate the mass that radiates at the post-collision Lorentz factor. Gat et al. (2013) argue that this could lead to overestimates of the flux at the interface between the shocked wind and the hydrogen shell, and hence a flare when none should exist.

The Gat et al. (2013) model accounts for the radial structure of the jet when modeling the passage of the reverse shock through the original forward shock during a collision with a density jump. But their model does not resolve the density structure at the inner surface of a shell. It instead treats the inner surface as a single density jump of factor $a = 10^5$. The radial structure of a jet that has collided with a single jump a is not the same as for a jet that has traversed a series of smaller jumps that sum up to a. Indeed, when we apply our model to the jets and density profiles in Gat et al. (2013), it does not produce any flares either.

Figure 8 shows the radial structure of a jet after it has crashed into the 5 $M_\odot$ He merger shell in our study. The jet does not instantaneously transition into the shell, but instead encounters a series of density jumps over $\sim$ 2 hours. Consequently, the structure of the jet becomes highly complex, with the vast majority of the swept-up mass being confined to a narrow region at the leading edge of the jet. The potential smearing out of flares due to the radial extent of the jet is therefore far less than that predicted by the Gat et al. (2013) model. A relativistic blast wave colliding with this massive shell will thus produce a flare, even though the reverse shock and the curvature of the blast wave may reduce its amplitude.

6. CONCLUSION

Pop III GRBs, together with other primordial SNe (Whalen et al. 2008b; Fryer et al. 2010; Kasen et al. 2011; Tominaga et al. 2011; Hummel et al. 2012; Tanaka et al. 2012; Meiksin & Whalen 2013; Pan et al. 2012; Frey et al. 2013; Moriya et al. 2013; Whalen et al. 2013a,b,c,e,f; Johnson et al. 2013a; Whalen et al. 2013h; Johnson et al. 2012; Whalen et al. 2013g; de Souza et al. 2013, 2014; Whalen et al. 2013i,d; Chen et al. 2014c,b,a), will soon directly probe the properties of the first stars in the universe in X-rays, the NIR, and radio. GRBs will be easily distinguished from other SNe at this epoch by their prompt gamma emission, afterglow X-rays, relatively short-lived NIR profiles, and their appearance at later times in the radio. Their environments, and hence their progenitors, can be deduced to some degree from the structures of their light curves. The detection of Pop III GRB afterglows is crucial to pinpointing their redshifts, since at $z \sim 20$ there is no host galaxy from which to infer a redshift, and even at $z \sim 10$ - 15 the protogalaxy would probably be too dim to be observed. Our algorithm produces afterglow light curves that are in good agreement with past work but goes well beyond them, giving realistic afterglow profiles for GRBs due to He mergers and binary mergers, which have not been modeled until now.

Bursts in winds are easily separated from GRBs in H II regions by their much brighter NIR and X-ray fluxes at early times. They also peak in the radio at much later times, 1- 30 days versus at most ~ 1 day. GRBs from He mergers have unique light curves that are characterized by prominent flares and abrupt quenching at less than a day across all bands. GRBs from binary mergers have light curves that are similar to those in winds except at later times, when their flux is abruptly cut off by the collision of the jet with the shell. This feature will generally only be visible in the radio because the X-ray and NIR fluxes will have fallen below the detection threshold of all current and proposed missions before they are cut off. The sudden drop in radio flux in this type of event is sometimes preceded by a flare. There is some degeneracy in energy and local environment with light curves across progenitor type that can complicate their classification, but in many cases it will still be possible to identify their progenitors.

Although Pop III GRBs at $z \sim 20$ can be detected by *Swift* and VLA today, identifying them as being primordial can be problematic because:

1. a Pop III GRB cannot necessarily be distinguished from an event at low redshift from the duration of its prompt gamma emission, which would be cosmologically dilated in time by factors of up to 20. These times can still fall well within the wide range of prompt emission times found for GRBs in the local universe today.

2. even if prompt emission is suspected to be from a primordial event, its NIR afterglow, which could confirm its redshift, would not be visible to most facilities today, and may be too transient to be captured by those that can detect them.

3. if prompt gamma emission is suspected to be from a Pop III GRB, it may not be accompanied by a radio afterglow that is strong enough to determine its redshift (only $\sim 10\%$ of GRBs have measurable radio signatures).

Some of these problems would persist even with the next generation of NIR and radio observatories. For example, if *Swift* detected a burst that was thought to be Pop III, its NIR signature would disappear before *JWST* or a ground-based extremely large telescope could be tasked to observe it if it is a He merger event. Indeed, in spite of its extreme sensitivity in the NIR, *JWST* will probably not be used to follow up on future GRBs because doing so would rapidly deplete its limited fuel supply. GRB rates at $z \sim 20$ would also be so low that it is highly unlikely that the narrow *JWST* fields would encounter one in routine surveys over its mission lifetime.

Future successors to *Swift* such as EXIST and JANUS will be the best equipped to hunt for Pop III GRBs for two reasons:

1. they will be all-sky X-ray and NIR missions whose wide fields will partly compensate for the low GRB rates at $z \gtrsim 10$ predicted by some studies.

2. their onboard telescopes will be able to measure the NIR flux of a Pop III GRB from the moment of the burst, thereby determining its redshift and, in some cases, progenitor type.

For example, GRBs due to He mergers would, in all likelihood, only be detected by missions with onboard NIR telescopes. Our models show that NIR instruments with the sensitivity of the EXIST IRT would detect even the least energetic events at $z \sim 20$ but that the JANUS NIRT in some cases would not.

Our simulations also show that Pop III GRBs would appear in future NIR and radio surveys, regardless of prompt gamma emission. Radio afterglows at $z \sim 20$ would appear in ground-based campaigns by VLA and SKA with an appropriate cadence. These events could be easily be separated from the radio signatures of Pop III SNe, which evolve on much longer timescales (Meiksin & Whalen 2013). Further studies are needed to determine if Pop III GRBs and SNe can be distinguished from the many foreground sources of synchrotron emission that could contaminate their signal. Equally important, most Pop III GRBs are bright enough to appear in all-sky surveys at $z \sim 20$ by WFIRST and the Wide-Field Imaging Surveyor for High Redshift (WISH). The large search areas of these missions could compensate for the low event numbers at such redshifts. It should be noted that although Pop III GRBs may be more visible in the NIR than in the radio, radio facilities exist that are capable of seeing them now.

Hypernovae (HNe), highly energetic Type Ib/c SNe, may be associated with some Pop III GRBs. But new studies show that if the GRB is visible, it will completely outshine the HN (Smidt et al. 2014). If not, the HN itself will only be visible to *JWST* out to $z \sim 10$ - 15, the era of first galaxy formation, and to WFIRST at $z \sim 4$ - 6, the end of reionization. In the upper limit that there is a HN with every GRB, the HN rate would be ~ 100 times the detected GRB rate at a given redshift for typical opening angles for the jet. Even at these rates, it is unlikely that the HN would be found by *JWST* or the next generation of ELTs without its GRB first being detected, and they lie beyond the reach of all-sky NIR missions at $z \gtrsim 6$, which might otherwise have detected them because of their wide fields. But if the GRB is detected at $z \lesssim 15$, followup observations might reveal a HN.

Our suite of Pop III GRB light curves is not comprehensive. First, they do not account for multidimensional structures in the vicinity of the burst. Massive shells ejected in mergers are prone to dynamical instabilities that could fracture them into clumps, and emission from a relativistic jet crashing into a clump would be quite different than if it were piercing a crack in the shell. Second, as noted earlier, the ambient medium of the burst could be intermediate to the four canonical cases considered here. Clumps might exist in H II regions in the absence of winds, and GRB jets could break out along an axis perpendicular to the plane of a toroidal ejection. Finally, new models such as high-resolution special-relativistic hydrodynamics and particle-in-cell (PIC) simulations are needed to better probe the microphysical processes that contribute to the afterglow flux. Future multidimensional simulations in this vein can also address the imprint of realistic circumburst structures on the afterglows of Pop III GRBs.

RM was supported by LANL IGPP grant 10-150. D.J.W. was supported by the European Research Council under the European Community's Seventh Framework Programme (FP7/2007 - 2013) via the ERC Advanced Grant "STARLIGHT: Formation of the First Stars" (project number 339177). Work at LANL was done under the auspices of the National Nuclear Security Administration of the U.S. Department of Energy at Los Alamos National Laboratory under Contract No. DE-AC52-06NA25396. All ZEUS-MP simulations were performed with allocations from Institutional Computing (IC) on the Pinto cluster at LANL.

REFERENCES

Abel, T., Wise, J. H., & Bryan, G. L. 2007, ApJ, 659, L87
Baraffe, I., Heger, A., & Woosley, S. E. 2001, ApJ, 550, 890
Barkana, R. & Loeb, A. 2004, ApJ, 601, 64
Beers, T. C. & Christlieb, N. 2005, ARA&A, 43, 531
Blandford, R. D. & McKee, C. F. 1976, Physics of Fluids, 19, 1130
Bromm, V. & Loeb, A. 2002, ApJ, 575, 111
Bromm, V. & Loeb, A. 2006a, in American Institute of Physics Conference Series, Vol. 836, Gamma-Ray Bursts in the Swift Era, ed. S. S. Holt, N. Gehrels, & J. A. Nousek, 503–512
—. 2006b, ApJ, 642, 382
Bromm, V., Yoshida, N., Hernquist, L., & McKee, C. F. 2009, Nature, 459, 49
Burrows, D. N., Roming, P. W. A., Fox, D. B., Herter, T. L., Falcone, A., Bilén, S., Nousek, J. A., & Kennea, J. A. 2010, in Presented at the Society of Photo-Optical Instrumentation Engineers (SPIE) Conference, Vol. 7732, Society of Photo-Optical Instrumentation Engineers (SPIE) Conference Series
Caffau, E., Bonifacio, P., François, P., Spite, M., Spite, F., Zaggia, S., Ludwig, H.-G., Steffen, M., Mashonkina, L., Monaco, L., Sbordone, L., Molaro, P., Cayrel, R., Plez, B., Hill, V., Hammer, F., & Randich, S. 2012, A&A, 542, A51
Chen, K.-J., Heger, A., Woosley, S., Almgren, A., & Whalen, D. 2014a, arXiv:1402.5960
Chen, K.-J., Heger, A., Woosley, S., Almgren, A., Whalen, D., & Johnson, J. 2014b, arXiv:1402.4777
Chen, K.-J., Woosley, S., Heger, A., Almgren, A., & Whalen, D. 2014c, arXiv:1402.4134
Ciardi, B. & Loeb, A. 2000, ApJ, 540, 687
Clark, P. C., Glover, S. C. O., Smith, R. J., Greif, T. H., Klessen, R. S., & Bromm, V. 2011, Science, 331, 1040
Cucchiara, A., Levan, A. J., Fox, D. B., Tanvir, N. R., Ukwatta, T. N., Berger, E., Krühler, T., Küpcü Yoldaş, A., Wu, X. F., Toma, K., Greiner, J., Olivares, F. E., Rowlinson, A., Amati, L., Sakamoto, T., Roth, K., Stephens, A., Fritz, A., Fynbo, J. P. U., Hjorth, J., Malesani, D., Jakobsson, P., Wiersema, K., O'Brien, P. T., Soderberg, A. M., Foley, R. J., Fruchter, A. S., Rhoads, J., Rutledge, R. E., Schmidt, B. P., Dopita, M. A., Podsiadlowski, P., Willingale, R., Wolf, C., Kulkarni, S. R., & D'Avanzo, P. 2011, ApJ, 736, 7
Dai, Z. G., Huang, Y. F., & Lu, T. 1999, ApJ, 520, 634
Dai, Z. G. & Lu, T. 2002, ApJ, 565, L87
de Souza, R. S., Ishida, E. E. O., Johnson, J. L., Whalen, D. J., & Mesinger, A. 2013, MNRAS, 436, 1555
de Souza, R. S., Ishida, E. E. O., Whalen, D. J., Johnson, J., & Ferrara, A. 2014, arXiv:1401.2995
de Souza, R. S., Yoshida, N., & Ioka, K. 2011, A&A, 533, A32
Falcone, A. D., Burrows, D. N., Barthelmy, S., Chang, W., Fredley, J., Kelly, M., Klar, R., Palmer, D., Persyn, S., Reichard, K., Roming, P., Seifert, E., Smith, R. W. M., Wood, P., & Zugger, M. 2009, in Society of Photo-Optical Instrumentation Engineers (SPIE) Conference Series, Vol. 7435, Society of Photo-Optical Instrumentation Engineers (SPIE) Conference Series
Fenimore, E. E., Madras, C. D., & Nayakshin, S. 1996, ApJ, 473, 998
Frebel, A., Aoki, W., Christlieb, N., Ando, H., Asplund, M., Barklem, P. S., Beers, T. C., Eriksson, K., Fechner, C., Fujimoto, M. Y., Honda, S., Kajino, T., Minezaki, T., Nomoto, K., Norris, J. E., Ryan, S. G., Takada-Hidai, M., Tsangarides, S., & Yoshii, Y. 2005, Nature, 434, 871
Frey, L. H., Even, W., Whalen, D. J., Fryer, C. L., Hungerford, A. L., Fontes, C. J., & Colgan, J. 2013, ApJS, 204, 16
Fryer, C. L., Belczynski, K., Berger, E., Thöne, C., Ellinger, C., & Bulik, T. 2013, ApJ, 764, 181
Fryer, C. L. & Heger, A. 2005, ApJ, 623, 302
—. 2011, Astronomische Nachrichten, 332, 408
Fryer, C. L., Mazzali, P. A., Prochaska, J., Cappellaro, E., Panaitescu, A., Berger, E., van Putten, M., van den Heuvel, E. P. J., Young, P., Hungerford, A., Rockefeller, G., Yoon, S.-C., Podsiadlowski, P., Nomoto, K., Chevalier, R., Schmidt, B., & Kulkarni, S. 2007, PASP, 119, 1211
Fryer, C. L., Whalen, D. J., & Frey, L. 2010, in American Institute of Physics Conference Series, Vol. 1294, American Institute of Physics Conference Series, ed. D. J. Whalen, V. Bromm, & N. Yoshida, 70–75
Fryer, C. L. & Woosley, S. E. 1998, ApJ, 502, L9
Fryer, C. L., Woosley, S. E., & Hartmann, D. H. 1999, ApJ, 526, 152
Fryer, C. L., Woosley, S. E., & Heger, A. 2001, ApJ, 550, 372
Gat, I., van Eerten, H., & MacFadyen, A. 2013, ApJ, 773, 2
Glover, S. 2013, in Astrophysics and Space Science Library, Vol. 396, Astrophysics and Space Science Library, ed. T. Wiklind, B. Mobasher, & V. Bromm, 103
Gorenstein, P. 2011, in Society of Photo-Optical Instrumentation Engineers (SPIE) Conference Series, Vol. 8147, Society of Photo-Optical Instrumentation Engineers (SPIE) Conference Series
Gou, L. J., Mészáros, P., Abel, T., & Zhang, B. 2004, ApJ, 604, 508
Greif, T. H., Bromm, V., Clark, P. C., Glover, S. C. O., Smith, R. J., Klessen, R. S., Yoshida, N., & Springel, V. 2012, MNRAS, 424, 399
Greiner, J., Krühler, T., Fynbo, J. P. U., Rossi, A., Schwarz, R., Klose, S., Savaglio, S., Tanvir, N. R., McBreen, S., Totani, T., Zhang, B. B., Wu, X. F., Watson, D., Barthelmy, S. D., Beardmore, A. P., Ferrero, P., Gehrels, N., Kann, D. A., Kawai, N., Yoldaş, A. K., Mészáros, P., Milvang-Jensen, B., Oates, S. R., Pierini, D., Schady, P., Toma, K., Vreeswijk, P. M., Yoldaş, A., Zhang, B., Afonso, P., Aoki, K., Burrows, D. N., Clemens, C., Filgas, R., Haiman, Z., Hartmann, D. H., Hasinger, G., Hjorth, J., Jehin, E., Levan, A. J., Liang, E. W., Malesani, D., Pyo, T.-S., Schulze, S., Szokoly, G., Terada, K., & Wiersema, K. 2009, ApJ, 693, 1610
Greiner, J., Mannheim, K., Aharonian, F., Ajello, M., Balasz, L. G., Barbiellini, G., Bellazzini, R., Bishop, S., Bisnovatij-Kogan, G. S., Boggs, S., Bykov, A., DiCocco, G., Diehl, R., Elsässer, D., Foley, S., Fransson, C., Gehrels, N., Hanlon, L., Hartmann, D., Hermsen, W., Hillebrandt, W., Hudec, R., Iyudin, A., Jose, J., Kadler, M., Kanbach, G., Klamra, W., Kiener, J., Klose, S., Kreykenbohm, I., Kuiper, L. M., Kylafis, N., Labanti, C., Langanke, K., Langer, N., Larsson, S., Leibundgut, B., Laux, U., Longo, F., Maeda, K., Marcinkowski, R., Marisaldi, M., McBreen, B., McBreen, S., Meszaros, A., Nomoto, K., Pearce, M., Peer, A., Pian, E., Prantzos, N., Raffelt, G., Reimer, O., Rhode, W., Ryde, F., Schmidt, C., Silk, J., Shustov, B. M., Strong, A., Tanvir, N., Thielemann, F.-K., Tibolla, O., Tierney, D., Trümper, J., Varshalovich, D. A., Wilms, J., Wrochna, G., Zdziarski, A., & Zoglauer, A. 2012, Experimental Astronomy, 34, 551
Grindlay, J. E. 2010, in American Institute of Physics Conference Series, Vol. 1279, American Institute of Physics Conference Series, ed. N. Kawai & S. Nagataki, 212–219
Heger, A. & Woosley, S. E. 2002, ApJ, 567, 532
Hirano, S., Hosokawa, T., Yoshida, N., Umeda, H., Omukai, K., Chiaki, G., & Yorke, H. W. 2013, arXiv:1308.4456
Hong, J., Grindlay, J. E., Allen, B., Barthelmy, S. D., Skinner, G. K., & Gehrels, N. 2009, in Society of Photo-Optical Instrumentation Engineers (SPIE) Conference Series, Vol. 7435, Society of Photo-Optical Instrumentation Engineers (SPIE) Conference Series
Hosokawa, T., Omukai, K., Yoshida, N., & Yorke, H. W. 2011, Science, 334, 1250
Huang, Y., Dai, Z., & Lu, T. 1999, MNRAS, 309, 513

Huang, Y. F., Gou, L. J., Dai, Z. G., & Lu, T. 2000, ApJ, 543, 90
Hummel, J. A., Pawlik, A. H., Milosavljević, M., & Bromm, V. 2012, ApJ, 755, 72
Inoue, S., Omukai, K., & Ciardi, B. 2007, MNRAS, 380, 1715
Ioka, K. 2003, ApJ, 598, L79
Ioka, K. & Mészáros, P. 2005, ApJ, 619, 684
Jeon, M., Pawlik, A. H., Greif, T. H., Glover, S. C. O., Bromm, V., Milosavljević, M., & Klessen, R. S. 2012, ApJ, 754, 34
Joggerst, C. C., Almgren, A., Bell, J., Heger, A., Whalen, D., & Woosley, S. E. 2010, ApJ, 709, 11
Joggerst, C. C. & Whalen, D. J. 2011, ApJ, 728, 129
Johnson, J. L., Whalen, D. J., Even, W., Fryer, C. L., Heger, A., Smidt, J., & Chen, K.-J. 2013a, arXiv:1304.4601
Johnson, J. L., Whalen, D. J., Fryer, C. L., & Li, H. 2012, ApJ, 750, 66
Johnson, J. L., Whalen, D. J., Li, H., & Holz, D. E. 2013b, ApJ, 771, 116
Kasen, D., Woosley, S. E., & Heger, A. 2011, ApJ, 734, 102
Kashiyama, K., Nakauchi, D., Suwa, Y., Yajima, H., & Nakamura, T. 2013, ApJ, 770, 8
Keller, S. C., Bessell, M. S., Frebel, A., Casey, A. R., Asplund, M., Jacobson, H. R., Lind, K., Norris, J. E., Yong, D., Heger, A., Magic, Z., da Costa, G. S., Schmidt, B. P., & Tisserand, P. 2014, Nature, 506, 463
Kitayama, T., Yoshida, N., Susa, H., & Umemura, M. 2004, ApJ, 613, 631
Lamb, D. Q. & Reichart, D. E. 2000, ApJ, 536, 1
Laskar, T., Berger, E., Tanvir, N., Zauderer, B. A., Margutti, R., Levan, A., Perley, D., Fong, W.-f., Wiersema, K., Menten, K., & Hrudkova, M. 2014, ApJ, 781, 1
Latif, M. A., Schleicher, D. R. G., Schmidt, W., & Niemeyer, J. 2013, MNRAS, 433, 1607
MacFadyen, A. I., Woosley, S. E., & Heger, A. 2001, ApJ, 550, 410
Meiksin, A. & Whalen, D. J. 2013, MNRAS, 430, 2854
Mesler, R. A., Whalen, D. J., Lloyd-Ronning, N. M., Fryer, C. L., & Pihlström, Y. M. 2012, ApJ, 757, 117
Mészáros, P. & Rees, M. J. 2010, ApJ, 715, 967
Moderski, R., Sikora, M., & Bulik, T. 2000, ApJ, 529, 151
Moriya, T. J., Blinnikov, S. I., Tominaga, N., Yoshida, N., Tanaka, M., Maeda, K., & Nomoto, K. 2013, MNRAS, 428, 1020
Nagakura, H., Suwa, Y., & Ioka, K. 2012, ApJ, 754, 85
Nakar, E. & Granot, J. 2007, MNRAS, 380, 1744
Nakauchi, D., Suwa, Y., Sakamoto, T., Kashiyama, K., & Nakamura, T. 2012, ApJ, 759, 128
Pan, T., Kasen, D., & Loeb, A. 2012, MNRAS, 422, 2701
Panaitescu, A. & Kumar, P. 2000, ApJ, 543, 66
Panaitescu, A. & Meszaros, P. 2000, Astrophysical Journal Letters, 544
Passy, J.-C., De Marco, O., Fryer, C. L., Herwig, F., Diehl, S., Oishi, J. S., Mac Low, M.-M., Bryan, G. L., & Rockefeller, G. 2012, ApJ, 744, 52
Paul, J., Wei, J., Basa, S., & Zhang, S.-N. 2011, Comptes Rendus Physique, 12, 298
Pawlik, A. H., Milosavljević, M., & Bromm, V. 2013, ApJ, 767, 59
Pe'er, A. 2012, ApJ, 752, L8
Ritter, J. S., Safranek-Shrader, C., Gnat, O., Milosavljević, M., & Bromm, V. 2012, ApJ, 761, 56
Roming, P. W. A., Pritchard, T. A., Prieto, J. L., Kochanek, C. S., Fryer, C. L., Davidson, K., Humphreys, R. M., Bayless, A. J., Beacom, J. F., Brown, P. J., Holland, S. T., Immler, S., Kuin, N. P. M., Oates, S. R., Pogge, R. W., Pojmanski, G., Stoll, R., Shappee, B. J., Stanek, K. Z., & Szczygiel, D. M. 2012, ApJ, 751, 92
Rybicki, G. & Lightman, A. 1979, Radiative Processes in Astrophysics (New York: Wiley-Interscience)
Safranek-Shrader, C., Milosavljevic, M., & Bromm, V. 2013, arXiv:1307.1982
Salvaterra, R., Della Valle, M., Campana, S., Chincarini, G., Covino, S., D'Avanzo, P., Fernández-Soto, A., Guidorzi, C., Mannucci, F., Margutti, R., Thöne, C. C., Antonelli, L. A., Barthelmy, S. D., de Pasquale, M., D'Elia, V., Fiore, F., Fugazza, D., Hunt, L. K., Maiorano, E., Marinoni, S., Marshall, F. E., Molinari, E., Nousek, J., Pian, E., Racusin, J. L., Stella, L., Amati, L., Andreuzzi, G., Cusumano, G., Fenimore, E. E., Ferrero, P., Giommi, P., Guetta, D., Holland, S. T., Hurley, K., Israel, G. L., Mao, J., Markwardt, C. B., Masetti, N., Pagani, C., Palazzi, E., Palmer, D. M., Piranomonte, S., Tagliaferri, G., & Testa, V. 2009, Nature, 461, 1258
Sari, R., Piran, T., & R., N. 1998, ApJ, 497, L17
Smidt, J., Whalen, D. J., Even, W., Wiggins, B., Johnson, J. L., & Fryer, C. L. 2014, arXiv:1401.5837
Smith, B. D. & Sigurdsson, S. 2007, ApJ, 661, L5
Smith, B. D., Turk, M. J., Sigurdsson, S., O'Shea, B. W., & Norman, M. L. 2009, ApJ, 691, 441
Spergel, D., Gehrels, N., Breckinridge, J., Donahue, M., Dressler, A., Gaudi, B. S., Greene, T., Guyon, O., Hirata, C., Kalirai, J., Kasdin, N. J., Moos, W., Perlmutter, S., Postman, M., Rauscher, B., Rhodes, J., Wang, Y., Weinberg, D., Centrella, J., Traub, W., Baltay, C., Colbert, J., Bennett, D., Kiessling, A., Macintosh, B., Merten, J., Mortonson, M., Penny, M., Rozo, E., Savransky, D., Stapelfeldt, K., Zu, Y., Baker, C., Cheng, E., Content, D., Dooley, J., Foote, M., Goullioud, R., Grady, K., Jackson, C., Kruk, J., Levine, M., Melton, M., Peddie, C., Ruffa, J., & Shaklan, S. 2013, arXiv:1305.5425
Stacy, A., Bromm, V., & Loeb, A. 2011, MNRAS, 413, 543
Stacy, A., Greif, T. H., & Bromm, V. 2012, MNRAS, 422, 290
Stanek, K. Z., Matheson, T., Garnavich, P. M., Martini, P., Berlind, P., Caldwell, N., Challis, P., Brown, W. R., Schild, R., Krisciunas, K., Calkins, M. L., Lee, J. C. Hathi, N., Jansen, R. A., Windhorst, R., Echevarria, L., Eisenstein, D. J., Pindor, B. Olszewski, E. W., Harding, P., Holland, S. T., & Bersier, D. 2003, ApJ, 1, L17
Suwa, Y. & Ioka, K. 2011, ApJ, 726, 107
Tanaka, M., Moriya, T. J., Yoshida, N., & Nomoto, K. 2012, MNRAS, 422, 2675
Taylor, G. 1950, Royal Society of London Proceedings Series A, 201, 159
Taylor, G. B., Ellingson, S. W., Kassim, N. E., Craig, J., Dowell, J., Wolfe, C. N., Hartman, J., Bernardi, G., Clarke, T., Cohen, A., Dalal, N. P., Erickson, W. C., Hicks, B., Greenhill, L. J., Jacoby, B., Lane, W., Lazio, J., Mitchell, D., Navarro, R., Ord, S. M., Pihlström, Y., Polisensky, E., Ray, P. S., Rickard, L. J., Schinzel, F. K., Schmitt, H., Sigman, E., Soriano, M., Stewart, K. P., Stovall, K., Tremblay, S., Wang, D., Weiler, K. W., White, S., & Wood, D. L. 2012, Journal of Astronomical Instrumentation, 1, 50004
Toma, K., Sakamoto, T., & Mészáros, P. 2011, ApJ, 731, 127
Tominaga, N., Morokuma, T., Blinnikov, S. I., Baklanov, P., Sorokina, E. I., & Nomoto, K. 2011, ApJS, 193, 20
Totani, T. 1997, ApJ, 486, L71
Totani, T., Kawai, N., Kosugi, G., Aoki, K., Yamada, T., Iye, M., Ohta, K., & Hattori, T. 2006, PASJ, 58, 485
Turk, M. J., Abel, T., & O'Shea, B. 2009, Science, 325, 601
Wang, F. Y., Bromm, V., Greif, T. H., Stacy, A., Dai, Z. G., Loeb, A., & Cheng, K. S. 2012, ApJ, 760, 27
Wang, F.-Y., Qi, S., & Dai, Z.-G. 2011, MNRAS, 415, 3423
Whalen, D., Abel, T., & Norman, M. L. 2004, ApJ, 610, 14
Whalen, D. & Norman, M. L. 2006, ApJS, 162, 281
—. 2008a, ApJ, 673, 664
Whalen, D., Prochaska, J. X., Heger, A., & Tumlinson, J. 2008a, ApJ, 682, 1114
Whalen, D., van Veelen, B., O'Shea, B. W., & Norman, M. L. 2008b, ApJ, 682, 49
Whalen, D. J. 2012, arXiv:1209.4688
Whalen, D. J., Even, W., Frey, L. H., Smidt, J., Johnson, J. L., Lovekin, C. C., Fryer, C. L., Stiavelli, M., Holz, D. E., Heger, A., Woosley, S. E., & Hungerford, A. L. 2013a, ApJ, 777, 110
Whalen, D. J., Even, W., Lovekin, C. C., Fryer, C. L., Stiavelli, M., Roming, P. W. A., Cooke, J., Pritchard, T. A., Holz, D. E., & Knight, C. 2013b, ApJ, 768, 195
Whalen, D. J., Even, W., Smidt, J., Heger, A., Chen, K.-J., Fryer, C. L., Stiavelli, M., Xu, H., & Joggerst, C. C. 2013c, ApJ, 778, 17

Whalen, D. J., Even, W., Smidt, J., Heger, A., Hirschi, R., Yusof, N., Stiavelli, M., Fryer, C. L., Chen, K.-J., & Joggerst, C. C. 2013d, arXiv:1312.5360
Whalen, D. J. & Fryer, C. L. 2012, ApJ, 756, L19
Whalen, D. J., Fryer, C. L., Holz, D. E., Heger, A., Woosley, S. E., Stiavelli, M., Even, W., & Frey, L. H. 2013e, ApJ, 762, L6
Whalen, D. J., Joggerst, C. C., Fryer, C. L., Stiavelli, M., Heger, A., & Holz, D. E. 2013f, ApJ, 768, 95
Whalen, D. J., Johnson, J. L., Smidt, J., Heger, A., Even, W., & Fryer, C. L. 2013g, ApJ, 777, 99
Whalen, D. J., Johnson, J. L., Smidt, J., Meiksin, A., Heger, A., Even, W., & Fryer, C. L. 2013h, ApJ, 774, 64
Whalen, D. J. & Norman, M. L. 2008b, ApJ, 672, 287
Whalen, D. J., Smidt, J., Even, W., Woosley, S. E., Heger, A., Stiavelli, M., & Fryer, C. L. 2014, ApJ, 781, 106
Whalen, D. J., Smidt, J., Johnson, J. L., Holz, D. E., Stiavelli, M., & Fryer, C. L. 2013i, arXiv:1312.6330
Wijers, R. & Galama, T. 1999, ApJ, 523, 177
Wijers, R. A. M. J., Bloom, J. S., Bagla, J. S., & Natarajan, P. 1998, MNRAS, 294, L13
Wise, J. H., Turk, M. J., Norman, M. L., & Abel, T. 2012, ApJ, 745, 50
Woosley, S. E. 1993, ApJ, 405, 273
Woosley, S. E. & Bloom, J. S. 2006, ARA&A, 44, 507
Yoon, S.-C. & Langer, N. 2005, A&A, 443, 643
Yoon, S.-C., Langer, N., & Norman, C. 2006, A&A, 460, 199
Zhang, W. & Fryer, C. L. 2001, ApJ, 550, 357

APPENDIX

In the canonical fireball model, GRBs are highly relativistic jets that propagate adiabatically into an ambient medium, i.e., only a very small fraction of the total energy of the burst is radiated away by electrons. Our afterglow model is valid in both relativistic and non-relativistic regimes and can model emission from jets in a variety of circumstellar media, including dense shells. It is an extension to the method in M12, and now incorporates radiative blast waves, spherical emission and beaming, and inverse Compton scattering (but does not include pair production). Our method is an important improvement over past work in that we can now smoothly evolve energy conservation for the jet from its usual form (Equation (1) below) from the highly relativistic regime to mildly relativistic and Newtonian regimes (Equations (11) - (14) below) as the jet decelerates through shells and other abrupt dense obstacles in its path. Our method produces K band light curves for Pop III GRBs in uniform H II regions at $z \sim 20$ that are in excellent agreement with those of Gou et al. (2004). In what follows, primed quantities refer to the frame of the jet, unprimed quantities refer to the frame of the surrounding interstellar medium, and the subscript $\oplus$ refers to the Earth frame.

The GRB blast wave is modeled as a uniform jet with an initial half-opening angle θ_0 and Lorentz factor Γ_0. The kinetic energy of the jet can be determined from $E_{\rm iso,\gamma}$, Γ_0, and θ_0. Energy conservation yields the Lorentz factor of the jet, Γ, as it propagates through the external medium:

$$\frac{d\Gamma}{dm} = -\frac{\hat{\gamma}\left(\Gamma^2-1\right) - \left(\hat{\gamma}-1\right)\Gamma\beta^2}{M_{\rm ej} + \epsilon m + (1-\epsilon)m\left[2\hat{\gamma}\Gamma - \left(\hat{\gamma}-1\right)\left(1+\Gamma^{-2}\right)\right]}, \tag{1}$$

where $M_{\rm ej}$ is the initial mass of the jet ejecta, m is the total mass that has been swept up by the jet, $\beta = \left(1-\Gamma^{-2}\right)^{1/2}$ in the normalized bulk velocity, $\hat{\gamma} \simeq (4\Gamma+1)/(3\Gamma)$ is the adiabatic index (Huang et al. 2000), and ϵ is the radiative efficiency (Pe'er 2012). ϵ in turn is given by (Dai et al. 1999)

$$\epsilon = \epsilon_e \frac{{t'}_{\rm syn}^{-1}}{{t'}_{\rm syn}^{-1} + {t'}_{\rm exp}^{-1}}, \tag{2}$$

where ϵ_e is the fraction of the burst energy stored in the electrons, $t'_{\rm syn}$ is the synchrotron cooling time scale of the injected electrons, and $t'_{\rm exp}$ is the age of the remnant.

The high resolution of our profiles allows us to treat the density as constant across each grid point. In the canonical GRB model, the jet is also assumed to sweep up all the material in its path. The total mass swept up by the jet by the time it reaches grid point n is therefore approximately

$$m(r) = \frac{4}{3}\pi\left(\rho_1 r_1^3 + \sum_{i=2}^{n}\rho_i\left(r_i^3 - r_{i-1}^3\right)\right), \tag{3}$$

where r_i and ρ_i are the radius and density of the ith grid point, respectively. The time $t_{\rm obs}$ at which a photon emitted at the leading edge of the jet reaches an observer along the line of sight can be found by integrating Equation (12) from Huang et al. (1999):

$$t = \frac{1}{c}\int \frac{dr}{\beta\Gamma\left(\Gamma + \sqrt{\Gamma^2-1}\right)}, \tag{4}$$

where c is the speed of light.

As the jet propagates toward the observer, it also expands laterally at the comoving sound speed

$$c'_s = \frac{da'}{dt'} = \sqrt{\frac{\hat{\gamma}\left(\hat{\gamma}-1\right)\left(\Gamma-1\right)}{1+\hat{\gamma}\left(\Gamma-1\right)}}, \tag{5}$$

where a is the half the diameter of the leading edge of the jet. Transforming into the isotropic frame, we get

$$\frac{da'}{dt'} = \frac{1}{\Gamma}\frac{da}{dt}. \tag{6}$$

Because the jet half-opening angle $\theta_j = \arctan(a/r)$, the factor of $1/\Gamma$ in Equation (6) leads to a nearly constant value of θ_j until the Lorentz factor approaches $\Gamma = 1/\theta_j$, when the jet experiences rapid lateral expansion in the isotropic frame. It is somewhat standard practice to use the approximation $\theta_j \simeq a/r$, but this expression is not valid at late times, when θ_j can be greater than 30°.

At the onset of the afterglow, the jet can be modeled as a slab of thickness $\Delta = ct_{\rm B}$, where c is the speed of light and $t_{\rm B}$ is the isotropic frame burst duration. The thickness of the jet in the isotropic frame is related to its thickness in the comoving frame by $\Delta = \Delta'/\Gamma$. For a differential comoving frame time $\delta t'$, the evolution of the jet thickness is $\delta\Delta = c_s'\delta t'/\Gamma$. The relationship between $\delta t'$ and δt is $\delta t = \Gamma\delta t'$. Therefore, the isotropic frame jet thickness evolves as

$$\frac{d\Delta}{dt} = \frac{c_s'}{\Gamma^2} \tag{7}$$

Density Jumps

If the GRB jet encounters an abrupt change in the density of the surrounding medium, Equation (1), which assumes self-similar expansion of the ejecta, no longer applies. When the jet collides with the jump, a contact discontinuity forms between the material that was swept up by the jet prior to the collision and the material that was swept up afterwards. A reverse shock forms at the contact discontinuity and backsteps into the jet in the frame of the jet. A forward shock also forms just past the jump and propagates into the medium beyond it. The contact discontinuity also moves forward, but at a much lower velocity as the jet continues to advance into the new medium and plow it up.

Although several analytic treatments exist for the evolution of the jet and its component shocks at a density jump (Nakar & Granot 2007; Dai & Lu 2002; Gat et al. 2013), they all assume that the jet will be relativistic upon collision with the jump, which is not always true for our density profiles. We must therefore resort to the general Blandford & McKee (1976) and Taylor (1950) equations for the jump conditions in order to self-consistently evolve the jet evolution in any medium.

When the jet encounters a density jump, the medium surrounding the jump can be partitioned into four regions (Figure 9). Region I is the undisturbed material beyond the density jump. Region II is the postshock material behind the forward shock, region III is the region of the jet through which the reverse shock has passed, and region IV is the unshocked jet material. The contact discontinuity forms between regions II and III. For a relativistic or mildly-relativistic jet, the jump conditions follow from the conservation of energy ($w\gamma^2\beta$), momentum ($w\gamma^2\beta^2 + p$), and particle number ($n\gamma\beta$) flux densities across the jump in the frame of the shock, where w and p are the enthalpy and pressure of the gas, respectively, and γ and β are the Lorentz factor and velocity of the gas particles. The pressure of the gas is

$$p = (\hat{\gamma} - 1)(e - \rho), \tag{8}$$

where $\hat{\gamma}$ is the adiabatic index,$e = \gamma n m_p c^2$ is the energy density of the gas and $\rho = n m_p c^2$ is the rest-frame gas density. The enthalpy $w = e + p$.

For any two adjacent regions 1 and 2 in regions I-IV described above, the jump conditions for relativistic and mildly-relativistic jets are (Blandford & McKee 1976)

$$\frac{e_2}{n_2} = \gamma_2\frac{w_1}{n_1}, \tag{9}$$

$$\frac{n_2}{n_1} = \frac{\hat{\gamma_2}\gamma_2 + 1}{\hat{\gamma_2} - 1}, \tag{10}$$

and

$$\Gamma^2 = \frac{(\gamma_2 + 1)\left[\hat{\gamma_2}(\gamma_2 - 1) + 1\right]^2}{\hat{\gamma_2}(2 - \hat{\gamma_2})(\gamma_2 - 1) + 2}, \tag{11}$$

where Γ is the Lorentz factor of the new forward shock. There are three known quantities: the Lorentz factor of the jet when it crashes into the density jump and the densities n_I and n_{IV} of regions I and IV, respectively. From these three quantities and the requirement that the pressure and energy density must be equal in regions II and III (due to the presence of a contact discontinuity between them) the Lorentz factors of the forward shock, the reverse shock, and the contact discontinuity can be determined from the three jump conditions.

Given these Lorentz factors an infinitesimal time after the leading edge of the jet collides with the jump, the subsequent motion of the forward shock is determined from energy conservation with Equation (4) of Nakar & Granot (2007). The evolution of the reverse shock is set by the fact that the energy density remains constant across the contact discontinuity. The Lorentz factor that satisfies this requirement is found numerically. Meanwhile, the initial shock, which has no knowledge of the contact discontinuity, continues to expand adiabatically.

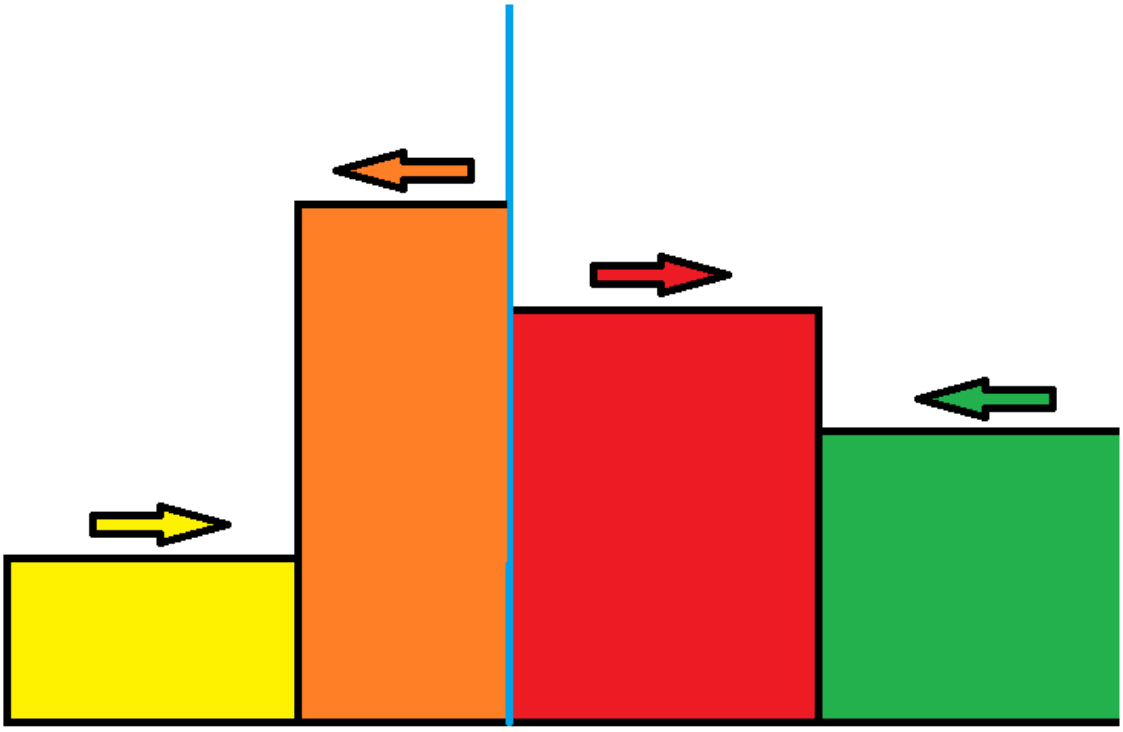

FIG. 9.— The interaction of a GRB jet with a density jump. The medium on either side of the jump can be broken into four regions: region I (green), the undisturbed material beyond the density jump, region II (red), the material that has been shocked by the forward shock, region III (orange), the region of the jet through which the reverse shock has passed, and region IV (yellow), the unshocked jet material. A contact discontinuity forms between regions II and III (blue line), effectively preventing the material in those two regions from mixing. The colored arrows show the direction of flow of the four regions in the frame of the contact discontinuity. The height of each colored block represents the density of that region (in arbitrary units).

Previous authors have assumed the jet to be relativistic when it encounters the jump. This in general is true for simple density profiles where one or perhaps a few density jumps are present. In our much more complicated and realistic profiles, however, there can be dozens of density jumps. If the jump scale factor $a = n/n_0$ (where n_0 and n are the densities of the medium before and after the jump, respectively) is > 1, the Lorentz factor of the new forward shock will usually be lower than that of the initial shock. If the new forward shock encounters a second density jump, then another forward shock will be produced with an even lower Lorentz factor. The forward shock can eventually become non-relativistic when it encounters a subsequent jump, and the Blandford-McKee conditions will no longer apply. The flow will instead obey the Sedov-von Neumann-Taylor jump conditions for a Newtonian fluid (Taylor 1950):

$$\frac{\rho_1}{\rho_0} = \frac{\hat{\gamma} - 1 + (\hat{\gamma} + 1)\, y_1}{\hat{\gamma} + 1 + (\hat{\gamma} - 1)\, y_1}, \tag{12}$$

$$\frac{U^2}{a^2} = \frac{1}{2\hat{\gamma}} \left[\hat{\gamma} - 1 + (\hat{\gamma} + 1)\, y_1\right], \tag{13}$$

and

$$\frac{u_1}{U} = \frac{2\,(y_1 - 1)}{\hat{\gamma} - 1 + (\hat{\gamma} + 1)\, y_1}, \tag{14}$$

where ρ_0 and ρ_1 are the densities before and after the jump, respectively, $\hat{\gamma} = 5/3$ is the adiabatic index, $y_1 = p_1/p_0$, p_0 and p_1 are the pressures behind and ahead of the jump, a is the sound speed, U is the velocity of the forward shock, and u_1 is the velocity of the fluid behind the forward shock. The velocities of the forward and reverse shocks and the contact discontinuity can be found by solving these jump conditions numerically if the velocity of the initial shock and the pressures of regions I and IV are known. Our ZEUS-MP models provide the temperature of region IV at each grid point, and the temperature of region I can be calculated by assuming equipartition of thermal and kinetic energies within the jet. The pressures in these regions are then easily obtained from the temperatures by the ideal gas law.

Our afterglow model in M12 essentially ignores the presence of density jumps and instead assumes that the evolution of the jet is dependent only on the total mass it sweeps up. The mass swept up by the jet is assumed to instantly mix with previously swept-up material, with a prompt change in the Lorentz factor along the entire jet. In reality, any collision with external structures produces a reverse shock that steps backward through the jet. Until the reverse

shock reaches a location in the jet, that location is not aware that any interaction has taken place. Consequently, any sharp feature in the light curve that might be produced by a density jump will be somewhat smoothed out by a time equal to the jet-crossing time of the reverse shock.

The Injection Break

If we assume that a constant fraction ϵ_B of the total fireball energy is stored in magnetic fields, then the equipartition magnetic field strength at the shock boundary is (i.e. Huang et al. 2000):

$$\frac{B'^2}{8\pi} = \epsilon_B \frac{\hat{\gamma}\Gamma + 1}{\hat{\gamma} - 1} (\Gamma - 1)\, n(r) m_p c^2, \tag{15}$$

where ϵ_B is the fraction of the burst energy stored in magnetic fields, $n(r)$ is the number density of the medium at radius r, and m_p is the proton mass.

The electrons that are injected into the shock are assumed to have a velocity distribution $N(\gamma) \propto \gamma^{-p}$ with a minimum Lorentz factor γ_m. The minimum Lorentz factor of the injected electrons is (Huang et al. 2000)

$$\gamma_m = \epsilon_e (\Gamma - 1) \frac{m_p (p-2)}{m_e (p-1)} + 1, \tag{16}$$

where m_e is the electron mass. Electrons with a Lorentz factor γ_e emit synchrotron radiation at a characteristic frequency (Rybicki & Lightman 1979)

$$\nu(\gamma_e) = \frac{\gamma}{1 - \beta_e} \frac{3 q_e B}{4\pi m_e c}, \tag{17}$$

where $\beta_e = \sqrt{1 - \gamma_e^{-2}}$, and q_e is the electron charge. The injection break frequency ν_m corresponds to the peak emission frequency of the injected electrons, and can be found by substituting $\gamma_e = \gamma_m$ into Equation (17).

The Cooling Break

Relativistic electrons in the shock cool radiatively through inverse Compton (IC) scattering and synchrotron emission on a comoving frame timescale (Panaitescu & Kumar 2000)

$$t'_{\rm rad}(\gamma) = \frac{t'_{\rm syn}}{Y + 1}, \tag{18}$$

where Y is the Compton parameter. The synchrotron cooling time scale $t'_{\rm syn}$ of an electron is equal to the ratio of its energy E to the synchrotron power P it radiates:

$$t'_{\rm syn} = \frac{E}{P} = \frac{1}{\gamma_e \beta_e^2} \frac{6\pi m_e c}{\sigma_T B'^2}, \tag{19}$$

where σ_T is the Thomson cross section for electron scattering. Equations (18) and (19) can be solved to find the Lorentz factor for electrons that cool on a timescale equal to the observer frame age of the remnant, γ_c:

$$\gamma_c = \frac{6\pi m_e c^2}{B'^2 \sigma_e (Y + 1) t'}. \tag{20}$$

The frequency of the cooling break, ν_c, is found by substituting $\gamma_e = \gamma_c$ in Equation (17).

Fast-Cooling Electrons

Electrons in the jet can also cool by adiabatic expansion of the gas. When cooling times for electrons with Lorentz factor γ_m are less than the age of the jet ($\nu_c < \nu_m$, where ν_c is the frequency of the cooling break), the electrons in the jet lose a significant portion of their energy through emission of radiation and are said to be radiative, or fast-cooling. On the other hand, if the cooling time is greater than the age of the jet ($\nu_c > \nu_m$) the electrons do not lose much energy to radiation and are said to be adiabatic, or slow-cooling.

To calculate Y, we only account for one upscattering of the synchrotron photons. If the electrons injected into the shock are fast-cooling and the frequency of the absorption break $\nu_a < \min(\nu_m, \nu_c)$, then Y is approximately (Panaitescu & Meszaros 2000)

$$Y_r = \gamma_{\rm m} \gamma_{\rm c} \tau_{\rm e}, \tag{21}$$

where a constant of order unity is ignored and τ_e, the optical depth to electron scattering, is

$$\tau'_e = \frac{\sigma_e m(r)}{4\pi m_{\rm p} r'^2}. \tag{22}$$

The medium becomes optically thick to synchrotron self-absorption at the absorption break frequency, ν_a. When both the injection break and the cooling break lie in the optically thick regime, Y becomes

$$Y_r = Y_* = \tau_e' \left(C_2^{2-p} \gamma_c^7 \gamma_m^{7(p-1)} \right)^{1/(p+5)}, \tag{23}$$

where $C_2 \equiv 5 q_e \tau_e' / \sigma_e B'$ (Panaitescu & Meszaros 2000).

Slow-Cooling Electrons

If the electrons are slow-cooling, Y becomes

$$Y_a = \tau_{\rm e}' \gamma_{\rm i}^{p-1} \gamma_{\rm c}^{3-p}, \tag{24}$$

as long as $\nu_a < \min(\nu_m, \nu_c)$ (Panaitescu & Meszaros 2000) and $1 < p < 3$ (here, we have again ignored a constant of order unity). If the injection and cooling breaks lie in the region of the spectrum that is optically thick to synchrotron self-absorption, then Y is the same as in the corresponding fast-cooling case and

$$Y_a = Y_*. \tag{25}$$

The Absorption Break

At lower frequencies, the medium in which the jet propagates becomes optically thick to synchrotron self-absorption. F_ν then becomes $\propto \nu^2$ at some absorption break frequency ν_a where the optical depth to self-absorption is $\tau_{\rm ab} = 1$. The frequency of the absorption break depends on the cooling regime of the electrons (fast or slow) and on the order and values of the injection and cooling breaks. In the fast-cooling regime (Panaitescu & Meszaros 2000),

$$\nu'_{\rm a,\ fast\text{-}cooling} = \begin{cases} C_2^{3/10} \gamma_c^{-1/2}, & \gamma_a < \gamma_c < \gamma_m \\ \left(C_2 \gamma_c \right)^{1/6}, & \gamma_c < \gamma_a < \gamma_m \\ \left(C_2 \gamma_c \gamma_m^{p-1} \right)^{1/(p+5)}, & \gamma_c < \gamma_m < \gamma_a, \end{cases} \tag{26}$$

and in the slow-cooling regime

$$\nu'_{\rm a,\ slow\text{-}cooling} = \begin{cases} C_2^{3/10} \gamma_m^{-1/2}, & \gamma_a < \gamma_m < \gamma_c \\ \left(C_2 \gamma_m^{p-1} \right)^{1/(p-4)}, & \gamma_m < \gamma_a < \gamma_c \\ \left(C_2 \gamma_m^{p-1} \gamma_c \right)^{1/(p+5)}, & \gamma_m < \gamma_c < \gamma_a. \end{cases} \tag{27}$$

Light Curves

In order to produce light curves, we must first find the time dependence of $\Gamma(r)$, $n(r)$, and $m(r)$. Equation (1) can be solved numerically for $\Gamma(r)$, and Equation (4) can then be used to relate the observer time $t_{\rm obs}$ to the jet position r, allowing us to rewrite the equations defining the three break frequencies in terms of $t_{\rm obs}$, $\Gamma(t_{\rm obs})$, $n(t_{\rm obs})$, and $M(t_{\rm obs})$. Given the three break frequencies and the peak flux density, analytical light curves can then be calculated from the radio to the γ-ray regions of the spectrum. If $\nu_a < \min(\nu_m, \nu_c)$, then the peak flux density $F_{\nu,\oplus}^{\rm max}$ occurs at the injection break if $\nu_{\rm m} < \nu_{\rm c}$ and at the cooling break if $\nu_{\rm m} > \nu_{\rm c}$:

$$F_{\nu,\oplus}^{\rm max} = \frac{\sqrt{3} \phi_{\rm p}}{4 \pi D^2} \frac{q_e^3 \beta_m^2}{m_{\rm e} c^2} \frac{\Gamma B' m(r)}{m_{\rm p}}, \tag{28}$$

where $\phi_{\rm p}$ is a factor calculated by Wijers & Galama (1999) that depends on the value of p, and $D = (1+z)^{-1/2} D_l$, where D_l is the luminosity distance to the source (Panaitescu & Kumar 2000). The flux at any frequency ν (ignoring relativistic beaming and the spherical nature of the emitting region) has been derived by Sari et al. (1998) and Panaitescu & Kumar (2000) as described below.

Fast-Cooling Electrons

When the electrons are in the fast-cooling regime, the peak flux occurs at the cooling break as long as $\nu_a < \nu_c$:

$$F_{\nu,\oplus} = F_{\nu,\oplus}^{\rm max} \begin{cases} (\nu/\nu_a)^2 (\nu_a/\nu_c)^{1/3}, & \nu < \nu_a \\ (\nu/\nu_c)^{1/3}, & \nu_a < \nu < \nu_c \\ (\nu/\nu_c)^{-1/2}, & \nu_c < \nu < \nu_m \\ (\nu/\nu_m)^{-p/2} (\nu_m/\nu_c)^{-1/2}, & \nu_m < \nu. \end{cases} \tag{29}$$

If the medium is optically thick to synchrotron self-absorption at the cooling break frequency, the maximum flux moves to the absorption break frequency. Between the absorption and cooling breaks, $F_\nu \propto \nu^{5/2}$ but becomes $\propto \nu^2$ below the cooling break:

$$F_{\nu,\oplus} = F_{\nu,\oplus}^{\max} \begin{cases} (\nu/\nu_c)^2(\nu_c/\nu_a)^{5/2}, & \nu < \nu_c \\ (\nu/\nu_a)^{5/2}, & \nu_c < \nu < \nu_a \\ (\nu/\nu_a)^{-1/2}, & \nu_a < \nu < \nu_m \\ (\nu/\nu_m)^{-p/2}(\nu_m/\nu_a)^{-1/2}, & \nu_m < \nu. \end{cases} \tag{30}$$

In canonical afterglow models that assume a uniform density environment, the cooling and injection breaks move to lower frequencies over time. Eventually, both can lie below the absorption break, but far too late in the evolution of the burst to be relevant to anything but the radio afterglow, and long after the time at which the electrons in the jet have transitioned to the slow-cooling regime. In the more realistic density profiles in our models, the extremely high density that the jet can encounter as it passes through a thick shell causes it to abruptly transition from highly relativistic to Newtonian expansion. The decrease in Γ leads to a sharp drop in the injection break frequency, while the increased density of the medium leads to a higher magnetic field amplitude, which in turn causes a drop in the cooling break frequency. The result is that the frequency of the absorption break can be several orders of magnitude higher than the cooling and injection break frequencies as the jet passes through the shell. Multiple transitions between the fast and slow electron cooling regimes can also occur. In a thick shell, when $\nu_a > \nu_m$ and the electrons are in the fast-cooling regime,

$$F_{\nu,\oplus} = F_{\nu,\oplus}^{\max} \begin{cases} (\nu/\nu_c)^2(\nu_c/\nu_a)^{5/2}, & \nu < \nu_c \\ (\nu/\nu_a)^{5/2}, & \nu_c < \nu < \nu_a \\ (\nu/\nu_a)^{-p/2}, & \nu_m < \nu. \end{cases} \tag{31}$$

Slow-Cooling Electrons

Our models yield the same flux as the canonical wind models until the jet collides with a shocked wind that has piled up behind a thick shell. If it does not reach the shocked wind in the first few hours, the electrons in the leading edge of the jet transition to the slow-cooling regime, with $\nu_a \ll \nu_m$ and

$$F_{\nu,\oplus} = F_{\nu,\oplus}^{\max} \begin{cases} (\nu/\nu_a)^2(\nu_a/\nu_m)^{1/3}, & \nu < \nu_a \\ (\nu/\nu_m)^{1/3}, & \nu_a < \nu < \nu_m \\ (\nu/\nu_m)^{-(p-1)/2}, & \nu_m < \nu < \nu_c \\ (\nu/\nu_c)^{-p/2}(\nu_c/\nu_m)^{-(p-1)/2}, & \nu_c < \nu. \end{cases} \tag{32}$$

If $\nu_m < \nu_a < \nu_c$,

$$F_{\nu,\oplus} = F_{\nu,\oplus}^{\max} \begin{cases} (\nu/\nu_m)^2(\nu_m/\nu_a)^{5/2}, & \nu < \nu_a \\ (\nu/\nu_a)^{5/2}, & \nu_a < \nu < \nu_m \\ (\nu/\nu_a)^{-(p-1)/2}, & \nu_m < \nu < \nu_c \\ (\nu/\nu_c)^{-p/2}(\nu_c/\nu_a)^{-(p-1)/2}, & \nu_c < \nu. \end{cases} \tag{33}$$

As noted above, as the jet passes through a dense shell, it can pass through multiple transitions between fast and slow electron cooling. When the electrons are in the slow-cooling regime and $\nu_a > \nu_c$,

$$F_{\nu,\oplus} = F_{\nu,\oplus}^{\max} \begin{cases} (\nu/\nu_m)^2(\nu_m/\nu_a)^{5/2}, & \nu < \nu_m \\ (\nu/\nu_a)^{5/2}, & \nu_m < \nu < \nu_a \\ (\nu/\nu_a)^{-p/2}, & \nu_a < \nu. \end{cases} \tag{34}$$

Inverse Compton Scattering

Low-frequency radiation can be boosted to higher energies in the presence of relativistic electrons through the process of inverse Compton (IC) scattering. The contribution to the light curve at any frequency ν can easily be determined by using the expressions for the synchrotron light curve at the IC frequency

$$\nu_{\rm IC} = \frac{\nu}{\Gamma^2\,(1+\beta^2)}. \tag{35}$$

The IC flux density at frequency ν is then

$$F_{\nu,\ {\rm IC}} = \tau_e F_{\nu_{\rm IC},\ {\rm syn}}, \tag{36}$$

where $F_{\nu_{\rm IC},\ {\rm syn}}$ is the synchrotron flux density at frequency $\nu_{\rm IC}$.

Spherical Emission and Beaming

The spherical nature of a GRB afterglow can substantially alter the observed light curve (Fenimore et al. 1996). The burst ejecta is initially ultra-relativistic, with $100 \lesssim \Gamma \lesssim 1000$. Radiation that is emitted by ejecta moving directly toward the observer (i.e., along the line connecting the observer and the progenitor) will be more highly beamed than radiation emitted by material that is not moving directly toward the observer. There will also be a delay in the arrival time of photons that are emitted from regions of the jet not traveling directly toward the observer, as these regions are further away from the observer. The beaming of radiation from material moving toward the observer leads to two effects. First, a higher flux is observed than would be expected if beaming was ignored. Second, the edge of the jet, which does not move directly toward the observer and is therefore not as highly beamed as the center of the jet, is not visible to the observer until $\Gamma \sim 1/\theta_j$. The delay in arrival time of light emitted by material not moving directly toward the observer tends to smooth out sharp features in the light curve of the jet. The method described above and in M12 neglects the spherical nature of the emitting region but can be slightly modified to account for it. The total luminosity $L'_{\nu'}$ radiated by the electrons at comoving frame frequency ν' must first be found. As shown by Wijers & Galama (1999), the power per unit frequency transforms as $P_\nu = \Gamma P'_{\nu'}$, implying that

$$L'_{\nu'} = 4\pi \frac{D^2 F_{\nu,\oplus}}{\Gamma}, \tag{37}$$

where D is the luminosity distance to the source and F_ν is the flux density detected at a distance D from the source by an observer in the isotropic frame if the spherical nature of the emitting region is neglected. The observed flux density is then

$$F_\nu = \frac{1}{4\pi D^2} \iint\limits_{\Omega_j} \frac{L'_{\nu'}[r(\theta)]\mathcal{D}^3}{\Omega_j} d\cos\theta \; d\phi, \tag{38}$$

where $\mathcal{D} = 1/\Gamma(1 - \beta\cos\theta)$ is the Doppler factor and $\Omega_j = 2\pi(1 - \cos\theta_j)$ is the solid angle subtended by the jet (Moderski et al. 2000). Equation (38) must be numerically integrated over the equal arrival time surface defined by

$$t = \int \frac{(1 - \beta\cos\theta)}{c\beta} dr = \text{constant}. \tag{39}$$

Let $(r(t), \theta)$ refer to a point on the leading edge of the jet, with $0 \leq \theta \leq \theta_j$ and $\theta = 0$ referring to the center of the jet and the direction to the observer. Radiation emitted by material at larger θ will be detected by the observer at progressively later times. For a given observer time t, the jet radius r at which radiation being detected from jet angle θ was emitted can be found by numerically integrating Equation (39) over r with θ held constant until the desired value of t is reached. Equation (38) is then used to find the total observed flux density by integrating over θ from 0 to θ_j. Note that, due to the large cosmological redshifts that we study, another correction must be made to transform the isotropic frame flux density at a given frequency to the reference frame of an earthbound observer.